2. Rationale for RFA of Oligometastasis and Oligo-Recurrence

Oligometastasis and oligo-recurrence, proposed by Niibe and Hayakawa [2], are the condition of one or a few metastatic or recurrent lesions without and with controlled primary tumor, respectively. Although significance of local therapy of metastatic lesions for survival benefit may be controversial, the International Registry of Lung Metastases (IRLM) [3] reported that 5-year overall survival for patients with complete resection of metastatic lung tumors was 36%, compared with 13% for patients without it. Further, for the patient for whom lung metastases were completely resected, survival depended on tumor number; that is, smaller number of metastases indicated better survival. Such data may suggest the rationale for applying local therapy including RFA for oligometastasis and oligo-recurrence. The registry also reported that the patients with disease-free intervals of 36 months or more had better prognosis. Thus, the patients with slow growing tumors are more appropriate candidates for RFA.

3. RFA of Primary Lung Cancer

There have been several studies on RFA in the management of primary lung cancers. In 2007, Simon et al. [4] reviewed 75 cases of previously untreated stage I NSCLC, resulting in overall survival of 78%, 57%, and 27% at 1, 2, and 5 years, respectively. Those results seemed to compare favorably with previous studies using external beam radiotherapy in similar stage tumors. Survival was significantly associated with tumor size, with approximately 50% of 5-year survival for the patients with tumors <3 cm. Further encouraging results were reported in a prospective multicenter study by Lencioni and coworkers [5]. Their study included 33 patients with NSCLC treated with RFA; of those, 13 patients had medically inoperable stage I NSCLC. The overall survival in patients with NSCLC was 70% and 48% at 1 and 2 years, respectively, with cancer-specific survival of 92% and 73% at 1 and 2 years. Subgroup analysis revealed 2-year overall survival of 75% and 2-year cancer-specific survival of 92% in patients with inoperable stage I NSCLC. Hiraki et al. [6] reported the outcomes of 27 patients with stage I NSCLC who were treated with RFA. During median follow-up period of 22 months, the mean survival time was 42 months. The overall survival and cancer-specific survival rates were 90% and 100% at 1 year, 84% and 93% at 2 years, and 74% and 83% at 3 years, respectively. Most recently, Hiraki et al. [7] have updated their data using 50 patients with stage I NSCLC. During median follow-up period of 37 months, a median survival time was 67 months, the overall, cancer-specific and disease-free survivals were 94%, 100%, and 82% at 1 year, 86%, 93%, and 64% at 2 years, and 74%, 80%, and 53% at 3 years, respectively. Despite favorable survival data, local progression was observed in 16 (31%) of the 52 tumors. Lanuti et al. [8] reported that during a median follow-up of 17 months, median survival time was 30 months for 31 patients; survaial rate was 85% at 1 year, 78% at 2 years, and 47% at 3 years; local progression rate was 32%. Pennathur et al. [9] reported that during a mean follow-up of 29 months, survival rate for 19 patients was 95% at 1 year, and 68% at 2 years; local progression rate was 42%.

With regard to oligo-recurrence of NSCLC, Kodama et al. [10] carried out an interesting study. Their study included 44 patients who underwent lung RFA for recurrent NSCLC after surgery. Forty-three patients had no extrapulmonary metastasis; one patient had liver and splenic metastasis, which was also treated with RFA. Single or multiple intrapulmonary recurrences were ablated. During mean follow-up period of 29 months, the overall survival rates were 98% at 1 year, 73% at 2 years, and 56% at 3 years. The recurrence-free survival rates were 77% at 1 year and 41% at 3 years. Tumor size and sex were independent significant predictors in the multivariate analysis. This study indicated that RFA may offer a chance of long-term survival for the patients with oligo-recurrence of primary lung cancer.

4. RFA of Metastatic Lung Cancer

4.1. Metastasis from Colorectal Cancer. The cancer that most frequently metastasizes to the lung is colorectal cancer. Approximately 10% of the patients who undergo curative resection for colorectal cancer develop lung metastases [11]. Standard treatment options include surgical resection and chemotherapy. Many surgeons believe that surgical resection is the best treatment that offers the potential for long-term survival in selected patients. Several large studies on pulmonary metastasectomy have demonstrated similar survival after surgery, with approximately 40% of the 5-year survival rate. Further, systematic review of 1684 patients by Pfannschmidt et al. [12] showed 48% of 5-year survival. However, patients with pulmonary metastases are often nonsurgical candidates because of other coexistent metastases, poor cardiopulmonary function, or refusal to undergo surgery. A recent chemotherapy regimen using fluorouracil and leucovorin with irinotecan or oxaliplatin has been shown to prolong survival, but the long-term results are still less than satisfactory, with a median survival of 14.8–21.5 months for the patients with metastatic colorectal cancer [13].

The prospective multicenter study by Lencioni et al. [5] showed that overall survival rate was 89% at 1 year and 66% at 2 years in patients with colorectal metastases; cancer-specific survival was 91% at 1 year and 68% at 2 years. Hiraki et al. [14] also assessed survival rates for 27 patients with pulmonary metastases from colorectal cancer. During the median follow-up period of 20.1 months after RFA, the overall survival rates were 96% at 1 year, 54% at 2 years, and 48% at 3 years. The most significant prognostic factor was the presence of extrapulmonary metastasis at the time of RFA. While patients with extrapulmonary metastasis never survived for 2 years, survival rates for patients without extrapulmonary metastasis were favorable, indicating 100% at 1 year, 76% at 2 years, and 68% at 3 years. These results showed the potential of long-term survival of the patients with oligo-recurrence from colorectal cancer with RFA. Yamakado et al. [15] reported the outcomes of a retrospective multicenter study on RFA for pulmonary metastases from colorectal cancer. The estimated 3-year survival rate was

46% for all patients. Extrapulmonary metastasis, tumor size, and the carcinoembryonic antigen level were significant prognostic factors in the univariate analysis. The first two factors were significantly independent prognostic factors in the multivariate analysis. Thirty-six patients with small lung metastases (< or =3 cm) and no extrapulmonary metastases had a 3-year survival rate of 78%. Yamakado et al. [16] also reported single center experiences of RFA for pulmonary metastases from colorectal cancer. For 78 patients, the 1-, 3-, and 5-year survival rates were 84%, 56%, and 35%, respectively, during a mean follow-up period of 25 months. The median survival time was 38.0 months. Univariate analysis revealed maximum tumor diameter of 3 cm or less, single-lung metastasis, lack of extrapulmonary metastasis, and normal carcinoembryonic antigen (CEA) level as better prognostic factors. The latter two were significant independent prognostic factors. The 1-, 3-, and 5-year survival rates were 97.7% (95% CI, 93.3–100%), 82.5% (95% CI, 68.2–96.8%), and 57.0% (95% CI, 34.7–79.2%) in 54 patients with no extrapulmonary metastases and 96.9% (95% CI, 90.8–100%), 86.1% (95% CI, 71.1–100%), and 62.5% (95% CI, 36.3–88.6%) in 33 patients with negative CEA levels. More recently, Chua et al. [17] reported promising long-term outcome obtained by a prospective trial of 108 patients with pulmonary metastases from colorectal cancer. The median survival reached 60 months, which appeared equivalent to data obtained by metastasectomy.

4.2. Metastasis from Hepatocellular Carcinoma. Hiraki et al. [18] performed a retrospective multicenter study on RFA for pulmonary metastases from hepatocellular carcinoma HCC. This study included 32 patients who had no intrahepatic recurrence or had treatable intrahepatic recurrence, who had no other metastases, and for whom RFA was performed with curative intent (i.e., not palliatively). The overall survival rates were 87% at 1 year and 57% at 2 and 3 years during a median follow-up period of 20.5 months. Median and mean survival times were 37.7 months and 43.2 months, respectively. Significantly better survival rates were obtained for patients with an absence of viable intrahepatic recurrence, Child-Pugh grade A, absence of liver cirrhosis, absence of hepatic C virus infection, and α-fetoprotein level of 10 ng/mL or lower at the time of RFA. These results seem to suggest that pulmonary metastasis from HCC is suitable candidates for RFA, if primary cancer is well controlled (i.e., oligo-recurrence).

4.3. Metastasis from Renal Cell Carcinoma. In cases of pulmonary metastases from renal cell carcinoma, patient survival was evaluated using data from 2 institutions [19]. This study included 39 nonsurgical candidates who were divided into 2 groups: a curative ablation group, which was formed by 15 patients with 6 or fewer lung metastases measuring ≤6 cm that were confined to the lung and who had all lung tumors ablated, and the palliative ablation group, which included 24 patients with extrapulmonary lesions, 7 or more lung tumors, or large tumors of >6 cm, and who had mass reduction. The overall survival rates in the curative and palliative ablation groups were 100% and 90% at 1 year, 100% and 52% at 3 years, and 100% and 52% at 5 years, respectively. The maximum lung tumor diameter was a significant prognostic factor.

4.4. Metastasis from Sarcoma. Palussière et al. [20] reported the outcomes of RFA for pulmonary metastases from various kinds of sarcoma. This study included 29 patients with a maximum of 5 lung metastases and without extrapulmonary metastasis (i.e., oligo-recurrence). During median follow-up period of 50 months, the 1- and 3-year survival rates were 92.2% and 65.2%, respectively. Median disease-free survival was 7 months. This study suggests that RFA may offer a chance for long-term survival for patients with oligo-recurrence from sarcoma, although the disease may recur in a relatively short-term followup.

Nakamura et al. [21] reported on RFA for 20 patients with pulmonary metastases from musculoskeletal sarcomas. During the mean follow-up period of 18 months (range, 7 months to 54 months), 9 of 20 patients died of lung tumor progression. The 1- and 3-year survival rates from RF ablation were 58% and 29% with a median survival time of 12.9 months in all patients. Survival rate for 14 patients with controlled primary tumor (33% at year) was not significantly different from that for 6 patients without controlled primary tumor (52% at 1 year). Survival rate for 10 patients with ≤5 lung metastases (38% at year) was not significantly different from that for 10 patients with >5 lung metastases (88% at 1 year). Thus, survival did not seem to depend on whether oligo-recurrence or not in the population that they studied.

5. Advantages and Limitations of RFA

Major limitation of RFA may be limited local efficacy. RFA induces various complications. Food and Drug Administration in the United States made a public announcement regarding deaths following RFA of lung tumors in 2007. Rare but serious complications may occur including bronchopleural fistula [22], pulmonary artery pseudoaneurysm [23], systemic air embolism [24], injury of the brachial nerve and the phrenic nerve [25, 26], pneumonia [27], and needle-tract seeding of cancer [28]. A case of fatal acute deterioration of interstitial pneumonia after RFA has been also reported [29]. Survey is required to recognize an incidence of acute deterioration after RFA in the patients with interstitial pneumonia and thereby to determine a role of RFA in such patients.

Notable advantages of RFA include limited influence on pulmonary function. According to a report by Ambrogi et al. [30], the mean forced vital capacity (VC) was 2.63 and 2.80 L at 1 and 3 months, respectively, compared with 2.91 L before RFA; the mean forced expiratory volume in 1 s (FEV(1)) was 1.71 and 1.86 L at 1 and 3 months, respectively, compared with 1.97 L before RFA. The multicenter prospective study by Lencioni et al. [5] also showed mean forced VC and FEV1 of 2.6 and 1.7 L, respectively, at 1 month, compared with 2.9 and 1.9 L, respectively, before RFA in 22 patients with non-small cell lung cancer. Tada et al. [31] reported that the mean VC and FEV(1) before RFA and 1 and 3 months after RFA were 3.04 and 2.24 L, 2.79 and 2.11 L, and 2.85 and 2.13 L,

respectively. De Baère et al. [32] reported that pulmonary function did not decrease after RFA; the mean VC and FEV1 were 2.9 and 2.2 L, respectively, after RFA, compared with 2.9 and 2.2 L, respectively, before RFA.

The freedom to perform the procedure regardless of any previous therapy is another important advantage. Adhesion after pulmonary surgery or radiation-induced pneumonitis is not an obstacle for performing the procedure. Thus, the procedure may be used as a salvage treatment for oligo-recurrence after surgery and radiation therapy. At the same time, RFA procedure is not an obstacle for performing concurrent or adjuvant chemotherapy or adjuvant radiation therapy. According to the Norton-Simon hypothesis [33], the effectiveness of chemotherapy agents is proportional to the growth rate of the tumor and the fastest tumor growth rates occur when tumors are not bulky. Therefore, if RFA can downsize the primary tumor, the remaining tumor cells may become more sensitive to chemotherapy. The combination with such therapeutic modalities is expected to increase the efficacy of RFA not only through an additive effect but also due to synergistic effects [34]. The availability to repeat procedures whenever required is also an important advantage. Although RFA results in relatively high rate of local failure, local failure may be salvaged by repetition of the procedure [35].

6. Conclusions

In conclusion, the early results of RFA for the treatment of patients with NSCLC and pulmonary metastasis from various primary cancers appear encouraging and suggest the potential to offer long-term survival for the patients with oligo-recurrence or oligometastasis of lung cancer. The usefulness of RFA for oligo-recurrence or oligometastasis of lung cancer should be clarified by prospective studies in the future.

Abbreviation

RFA: Radiofrequency ablation.

Conflict of Interests

The authors have no conflict of interests.

References

[1] D. E. Dupuy, R. J. Zagoria, W. Akerley, W. W. Mayo-Smith, P. V. Kavanagh, and H. Safran, "Technical innovation: percutaneous radiofrequency ablation of malignancies in the lung," *American Journal of Roentgenology*, vol. 174, no. 1, pp. 57–59, 2000.

[2] Y. Niibe and K. Hayakawa, "Oligometastases and oligo-recurrence: the new era of cancer therapy," *Japanese Journal of Clinical Oncology*, vol. 40, no. 2, Article ID hyp167, pp. 107–111, 2010.

[3] The International Registry of Lung Metastases, "Long-term results of lung metastasectomy: prognostic analyses based on 5206 cases," *The Journal of Thoracic and Cardiovascular Surgery*, vol. 113, pp. 37–49, 1997.

[4] C. J. Simon, D. E. Dupuy, T. A. DiPetrillo et al., "Pulmonary radiofrequency ablation: long-term safety and efficacy in 153 patients," *Radiology*, vol. 243, no. 1, pp. 268–275, 2007.

[5] R. Lencioni, L. Crocetti, R. Cioni et al., "Response to radiofrequency ablation of pulmonary tumours: a prospective, intention-to-treat, multicentre clinical trial (the RAPTURE study)," *The Lancet Oncology*, vol. 9, no. 7, pp. 621–628, 2008.

[6] T. Hiraki, H. Gobara, T. Iishi et al., "Percutaneous radiofrequency ablation for clinical stage I non-small cell lung cancer: results in 20 nonsurgical candidates," *Journal of Thoracic and Cardiovascular Surgery*, vol. 134, no. 5, pp. 1306–1312, 2007.

[7] T. Hiraki, H. Gobara, H. Mimura, Y. Matsui, S. Toyooka, and S. Kanazawa, "Percutaneous radiofrequency ablation of clinical stage i non-small cell lung cancer," *Journal of Thoracic and Cardiovascular Surgery*, vol. 142, no. 1, pp. 24–30, 2011.

[8] M. Lanuti, A. Sharma, S. R. Digumarthy et al., "Radiofrequency ablation for treatment of medically inoperable stage I non-small cell lung cancer," *Journal of Thoracic and Cardiovascular Surgery*, vol. 137, no. 1, pp. 160–166, 2009.

[9] A. Pennathur, J. D. Luketich, G. Abbas et al., "Radiofrequency ablation for the treatment of stage I non-small cell lung cancer in high-risk patients," *Journal of Thoracic and Cardiovascular Surgery*, vol. 134, no. 4, pp. 857–864, 2007.

[10] H. Kodama, K. Yamakado, H. Takaki et al., "Lung radiofrequency ablation for the treatment of unresectable recurrent non-small-cell lung cancer after surgical intervention," *CardioVascular and Interventional Radiology*, vol. 35, pp. 563–569, 2012.

[11] K. Shirouzu, H. Isomoto, A. Hayashi, Y. Nagamatsu, and T. Kakegawa, "Surgical treatment for patients with pulmonary metastases after resection of primary colorectal carcinoma," *Cancer*, vol. 76, pp. 393–398, 1995.

[12] J. Pfannschmidt, H. Dienemann, and H. Hoffmann, "Surgical resection of pulmonary metastases from colorectal cancer: a systematic review of published series," *Annals of Thoracic Surgery*, vol. 84, no. 1, pp. 324–338, 2007.

[13] H. Kelly and R. M. Goldberg, "Systemic therapy for metastatic colorectal cancer: current options, current evidence," *Journal of Clinical Oncology*, vol. 23, no. 20, pp. 4553–4560, 2005.

[14] T. Hiraki, H. Gobara, T. Iishi et al., "Percutaneous radiofrequency ablation for pulmonary metastases from colorectal cancer: midterm results in 27 patients," *Journal of Vascular and Interventional Radiology*, vol. 18, no. 10, pp. 1264–1269, 2007.

[15] K. Yamakado, S. Hase, T. Matsuoka et al., "Radiofrequency ablation for the treatment of unresectable lung metastases in patients with colorectal cancer: a multicenter study in Japan," *Journal of Vascular and Interventional Radiology*, vol. 18, no. 3, pp. 393–398, 2007.

[16] K. Yamakado, Y. Inoue, M. Takao et al., "Long-term results of radiofrequency ablation in colorectal lung metastases: single center experience," *Oncology Reports*, vol. 22, no. 4, pp. 885–891, 2009.

[17] T. C. Chua, A. Sarkar, A. Saxena, D. Glenn, J. Zhao, and D. L. Morris, "Long-term outcome of image-guided percutaneous radiofrequency ablation of lung metastases: an open-labeled prospective trial of 148 patients," *Annals of Oncology*, vol. 21, no. 10, pp. 2017–2022, 2010.

[18] T. Hiraki, K. Yamakado, O. Ikeda et al., "Percutaneous radiofrequency ablation for pulmonary metastases from hepatocellular carcinoma: results of a multicenter study in Japan," *Journal of Vascular and Interventional Radiology*, vol. 22, no. 6, pp. 741–748, 2011.

[19] N. Soga, K. Yamakado, H. Gohara et al., "Percutaneous radiofrequency ablation for unresectable pulmonary metastases from renal cell carcinoma," *BJU International*, vol. 104, no. 6, pp. 790–794, 2009.

[20] J. Palussière, A. Italiano, E. Descat et al., "Sarcoma lung metastases treated with percutaneous radiofrequency ablation: results from 29 patients," *Annals of Surgical Oncology*, vol. 18, pp. 3771–3777, 2011.

[21] T. Nakamura, A. Matsumine, K. Yamakado et al., "Lung radiofrequency ablation in patients with pulmonary metastases from musculoskeletal sarcomas: an initial experience (R#2)," *Cancer*, vol. 115, no. 16, pp. 3774–3781, 2009.

[22] J. Sakurai, T. Hiraki, T. Mukai et al., "Intractable pneumothorax due to bronchopleural fistula after radiofrequency ablation of lung tumors," *Journal of Vascular and Interventional Radiology*, vol. 18, no. 1, pp. 141–145, 2007.

[23] J. Sakurai, H. Mimura, H. Gobara, T. Hiraki, and S. Kanazawa, "Pulmonary artery pseudoaneurysm related to radiofrequency ablation of lung tumor," *CardioVascular and Interventional Radiology*, vol. 33, no. 2, pp. 413–416, 2010.

[24] T. Okuma, T. Matsuoka, S. Tutumi, K. Nakmura, and Y. Inoue, "Air embolism during needle placement for CT-guided radiofrequency ablation of an unresectable metastatic lung lesion," *Journal of Vascular and Interventional Radiology*, vol. 18, no. 12, pp. 1592–1594, 2007.

[25] T. Hiraki, H. Gobara, H. Mimura et al., "Brachial nerve injury caused by percutaneous radiofrequency ablation of apical lung cancer: a report of four cases," *Journal of Vascular and Interventional Radiology*, vol. 21, no. 7, pp. 1129–1133, 2010.

[26] Y. Matsui, T. Hiraki, H. Gobara et al., "Phrenic nerve injury after radiofrequency ablation of lung tumors: retrospective evaluation of the incidence and risk factors," *Journal of Vascular and Interventional Radiology*, vol. 23, pp. 780–785, 2012.

[27] T. Hiraki, H. Gobara, K. Kato, S. Toyooka, H. Mimura, and S. Kanazawa, "Bronchiolitis obliterans organizing pneumonia after radiofrequency ablation of lung cancer: report of three cases," *Journal of Vascular and Interventional Radiology*, vol. 23, pp. 126–130, 2012.

[28] T. Hiraki, H. Mimura, H. Gobara et al., "Two cases of needle-tract seeding after percutaneous radiofrequency ablation for lung cancer," *Journal of Vascular and Interventional Radiology*, vol. 20, no. 3, pp. 415–418, 2009.

[29] T. Okuma, T. Matsuoka, S. Hamamoto, K. Nakamura, and Y. Inoue, "Percutaneous computed tomography-guided radiofrequency ablation of lung tumors complicated with idiopathic interstitial pneumonia," *Annals of Thoracic Surgery*, vol. 87, no. 3, pp. 948–950, 2009.

[30] M. C. Ambrogi, M. Lucchi, P. Dini et al., "Percutaneous radiofrequency ablation of lung tumours: results in the mid-term," *European Journal of Cardio-thoracic Surgery*, vol. 30, no. 1, pp. 177–183, 2006.

[31] A. Tada, T. Hiraki, T. Iguchi et al., "Influence of radiofrequency ablation of lung cancer on pulmonary function," *CardioVascular and Intervention al Radiology*, vol. 35, pp. 860–867, 2012.

[32] T. De Baère, J. Palussière, A. Aupérin et al., "Midterm local efficacy and survival after radiofrequency ablation of lung tumors with minimum follow-up of 1 year: prospective evaluation," *Radiology*, vol. 240, no. 2, pp. 587–596, 2006.

[33] L. Norton and R. Simon, "The Norton-Simon hypothesis revisited," *Cancer Treatment Reports*, vol. 70, no. 1, pp. 163–169, 1986.

[34] M. Ahmed, M. Moussa, and S. N. Goldberg, "Synergy in cancer treatment between liposomal chemotherapeutics and thermal ablation," *Chemistry and Physics of Lipids*, vol. 165, pp. 424–437, 2012.

[35] T. Hiraki, H. Mimura, H. Gobara et al., "Repeat radiofrequency ablation for local progression of lung tumors: does it have a role in local tumor control?" *Journal of Vascular and Interventional Radiology*, vol. 19, no. 5, pp. 706–711, 2008.

Cancer Science
The official journal of the Japanese Cancer Association JCA

Comparative study of the value of dual tracer PET/CT in evaluating breast cancer

Ukihide Tateishi,[1,7] Takashi Terauchi,[2] Sadako Akashi-Tanaka,[3] Takayuki Kinoshita,[4] Daisuke Kano,[2] Hiromitsu Daisaki,[2] Takeshi Murano,[2] Hitoshi Tsuda[5] and Homer A. Macapinlac[6]

[1]Department of Radiology, Yokohama City University Graduate School of Medicine, Kanagawa; [2]Division of Screening Technology and Development, Research Center for Cancer Prevention and Screening, National Cancer Center, Tokyo; [3]Breast Oncology, Showa University School of Medicine, Tokyo; [4]Division of Breast Surgery and [5]Pathology and Clinical Laboratory Division, National Cancer Center Hospital, Tokyo, Japan; [6]Department of Nuclear Medicine, University of Texas, MD Anderson Cancer Center, Houston, Texas, USA

(Received April 9, 2012/Revised May 22, 2012/Accepted May 22, 2012/Accepted manuscript online May 28, 2012/Article first published online July 4, 2012)

The present study was conducted to assess the relationship between tumor uptake and pathologic findings using dual-tracer PET/computed tomography (CT) in patients with breast cancer. Seventy-four patients with breast cancer (mean age 54 years) who underwent ^{11}C-choline and 2-[^{18}F]fluoro-2-deoxy-D-glucose (^{18}F-FDG) PET/CT prior to surgery on the same day were enrolled in the present study. Images were reviewed by a board-certified radiologist and two nuclear medicine specialists who were unaware of any clinical information and a consensus was reached. Uptake patterns and measurements of dual tracers were compared with the pathologic findings of resected specimens as the reference standard. Mean (±SD) tumor size was 5.9 ± 3.2 cm. All primary tumors were identified on ^{18}F-FDG PET/CT and ^{11}C-choline PET/CT. However, ^{18}F-FDG PET/CT demonstrated focal uptake of the primary tumor with (n = 38; 51%) or without (n = 36; 49%) diffuse background breast uptake. Of the pathologic findings, multiple logistic regression analysis revealed an independent association between fibrocystic change and diffuse background breast uptake (odds ratio [OR] 8.57; 95% confidence interval [CI] 2.86–25.66; P < 0.0001). Tumors with higher histologic grade, nuclear grade, structural grade, nuclear atypia, and mitosis had significantly higher maximum standardized uptake values (SUV_{max}) and tumor-to-background ratios (TBR) for both tracers. Multiple logistic regression analysis revealed that only the degree of mitosis was independently associated with a high SUV_{max} (OR 7.45; 95%CI 2.21–25.11; P = 0.001) and a high TBR (OR 5.41; 95%CI 1.13–25.96; P = 0.035) of ^{11}C-choline PET/CT. In conclusion, ^{11}C-choline may improve tumor delineation and reflect tumor aggressiveness on PET/CT in patients with breast cancer. (*Cancer Sci* 2012; 103: 1701–1707)

Positron emission tomography/computed tomography (PET/CT) with the glucose analog 2-[^{18}F]fluoro-2-deoxy-D-glucose (^{18}F-FDG) is recognized as an important tool in initial tumor evaluation, including staging, in the evaluation of treatment response, and in the assessment of recurrent disease for breast cancer.[1,2] It has been reported that PET/CT adds incremental diagnostic confidence to PET in 60% of patients and in >50% of regions with increased ^{18}F-FDG uptake.[3] Tatsumi *et al.*[4] concluded that PET/CT was preferable in evaluating breast cancer lesions in view of the level of diagnostic confidence that it allows. Regardless of the exact type of PET/CT fusion technique, ^{18}F-FDG uptake in non-malignant conditions often leads to high background uptake on breast imaging.[5]

Histological changes are the cause of considerable variations and false-positive findings on breast imaging. Fibrocystic changes (FCC) are the most common of these conditions that can affect the assessment of imaging features on mammography[6,7] and MRI.[8,9] Similarly, there is evidence in the literature that ^{18}F-FDG PET and accelerated glucose metabolism as a result of FCC lead to false-positive findings and difficulty in determining the boundary of specificity.[10]

Choline is an essential component of the cell membrane and choline uptake is upregulated by choline kinase-α, which catalyses the phosphorylation of choline.[11,12] In mammary epithelial cells, levels of phosphocholine metabolites increase due to overexpression of choline kinase-α, which is regulated by the mitogen-activated protein kinase (MAPK) pathway.[11–13] Recent clinical studies in patients with breast carcinoma undergoing molecular-targeted therapy suggest that ^{11}C-choline uptake is 10-fold higher in aggressive breast carcinoma phenotypes and that the uptake of ^{11}C-choline on PET is correlated with tumor grade.[13] Thus, ^{11}C-choline is considered a promising radiotracer for the evaluation of breast cancer in the clinical setting prior to treatment.

Although both data from ^{18}F-FDG and ^{11}C-choline PET/CT allow more precise evaluation of the primary breast cancer, direct comparisons of these two tracers in breast cancer have not been made. In the present study, we sought to confirm and extend previous findings of ^{11}C-choline PET/CT studies by investigating the association between histological findings and the results of ^{18}F-FDG PET/CT investigations in patients with breast cancer.

Materials and Methods

Patients. Seventy-four patients (mean age 54 years; range 25–89 years) with breast carcinoma were enrolled in the present retrospective dual PET/CT study between March 2008 and March 2010. Patients were eligible for inclusion in the study if they met the following criteria: (i) performance status 0 or 1; (ii) no concomitant malignancy; (iii) histologically proven breast carcinoma diagnosed by biopsy at least 1 month before; and (iv) no history of hormone therapy. All patients were required to provide written informed consent. A regimen of 5-fluorouracil, epirubicin, and cyclophosphamide (FEC) plus paclitaxel was used as neoadjuvant chemotherapy in 32 patients (43%). As a rule, hormone therapy was introduced after completion of imaging studies if needed. Our institutional review board (National Cancer Center Hospital, Tokyo, Japan) approved the present study, which complied with the Health Insurance Portability and Accountability Act. The clinical records of all patients were available for review. All patients received surgery after imaging studies.

Phantom study. A phantom study of PET/CT was performed prior to the clinical study at two institutions to clarify the optimum conditions for data acquisition and to ensure quality control.[14] Studies were performed with a whole-body PET/CT

[7]To whom correspondence should be addressed.
E-mail: utateish@yokohama-cu.ac.jp

doi: 10.1111/j.1349-7006.2012.02348.x
© 2012 Japanese Cancer Association

scanner (Aquiduo PCA-7000B; Toshiba Medical Systems, Tochigi, Japan). The CT component of the scanner has a 16-row detector. We used an NEMA image quality (IQ) phantom (NU 2-2001) for cross calibration, because this type of phantom is used in many institutions and data regarding the estimation of the optimum time are available. The radioactivity concentration of the background was set at 2.6 ± 0.2 kBq/mL ^{18}F-FDG, similar to that in clinical settings. The radioactivity concentration of the hot portion was fourfold greater than that of the background. Data were collected over a period of 2–5 min in the dynamic acquisition mode and for 30 min in the static acquisition mode. The data acquired, including normalization data, cross-calibration data, blank scan data, and transmission data, were assessed for visual inspection, phantom noise equivalent count ($NEC_{phantom}$), percentage contrast ($Q_{H,10\ mm}$) and percentage background variability ($N_{10\ mm}$). The preferred parameters pertinent to the clinical condition were $NEC_{phantom} > 10.4$ (counts), $N_{10\ mm} < 6.2\%$, and $Q_{H10\ mm}/N_{10\ mm} > 1.9\%$. After a review of the data analyses, the optimum conditions for the PET/CT were determined as follows: data acquisition, 180 s for one bed; field-of-view, 500 mm; iteration, 4; subset, 14; matrix size,128 × 128; filter, Gaussian 8 mm in full width at half maximum; reconstruction, ordered-subsets expectation maximization (OSEM).

Data acquisition. ^{11}C-Choline was synthesized using a commercially available module, as described by Hara *et al.*[15] Prior to the ^{11}C-choline PET/CT study, patients fasted for at least 6 h. Immediately after they had evacuated their bladder, patients were placed in a supine, arm-up position. For the PET/CT, low-dose CT data were first acquired at 120 kVp using an autoexposure control system (beam pitch 0.875 or 1 and 1.5 or 2 mm × 16-row mode). Data acquisition was performed for each patient from the top of the skull to the mid-thigh. Patients maintained normal shallow respiration during the three-dimensional acquisition of CT scans. No iodinated contrast material was administered. Acquisition of emission scans from the head to the mid-thigh was started 5 min after intravenous administration of a mean ^{11}C-choline dose of 475 MBq (range 469–491 MBq). The ^{18}F-FDG PET/CT study was performed 1 h after the ^{11}C-choline PET/CT study in all patients. Patients received an intravenous injection of 311 MBq (range 197–397 MBq) ^{18}F-FDG with an uptake phase at 64 ± 5 min.

Image interpretation. Dedicated software (Vox-base SP1000 workstation; J-MAC Systems, Sapporo, Japan) was used to review all PET, CT, and coregistered PET/CT images in all standard planes. Images were analyzed visually and quantitatively by two independent reviewers, who recorded their findings after reaching a consensus. A region of interest (ROI) was outlined within areas of increased uptake and measured on each slice. When the lesion was extensively heterogeneous, the ROI was set so as to cover all the components of the lesion. The diffuse pattern of breast was assigned to the breast that shows homogeneous accumulation greater than aortic blood except for the primary lesion. For quantitative interpretations, the standardized uptake value (SUV) was determined according to the standard formula, with activity in the ROI recorded as Bq/mL per injected dose (Bq) per weight (kg), but time decay correction for whole-body image acquisition was not performed. The maximum SUV (SUV_{max}) was recorded using the maximum pixel activity within the ROI. The tumor-to-background ratio (TBR) was calculated with reference to uptake in the contralateral breast.

Pathologic analysis. All patients underwent surgery. Each tumor was staged according to the TNM classification of the International Union against Cancer.[16] Resected specimens were fixed in 10% buffered formalin and embedded in paraffin wax. Then, 4-μm sections were obtained in a plane perpendicular to the long axis of the breast. Paraffin-embedded microslices were stained with H&E. Tissue grading, nuclear grading, and structural grading were done using the grading system of Elston and Ellis.[17] Estrogen receptor (ER) and progesterone receptor status was evaluated using the H-scoring system of McCarty *et al.*[18] Human epidermal growth factor-2 (HER-2/neu) was evaluated by immunostaining with 4B5 primary antibody. Evaluation of the primary lesion was based on the following pathologic findings: FCC, differentiation, subtype, location, diameter of the invasive component, diameter of the non-invasive component, ratio of the invasive component in the tumor (%), tissue grading, nuclear grading, structural grading, nuclear atypia, mitosis, necrosis, fat invasion, cutaneous invasion, muscular invasion, ER status, progesterone receptor status, and HER-2/neu status. In the present study, "non-invasive component" referred to ductal carcinoma *in situ* (DCIS).

Statistical analysis. The Chi-squared test or Fisher's exact probability test were used to compare pathologic findings associated with PET/CT findings. In addition, the Wald test and 95% confidence intervals (CI) were used to evaluate the statistical significance of individual variables. To determine relationships of SUV and TBR between the two tracers, we used Spearman rank correlation. Comparisons of mean values between groups were made using Student's *t*-test or analysis of variance (ANOVA) with Bonferroni's adjustment for multiple comparisons. Parsimonious univariate and multivariate logistic regression models were used to measure independent associations with PET/CT findings. Statistical tests used a two-sided significance level of 0.05. Statistical analyses were performed using PASW Statistics 19 (IBM, Tokyo, Japan).

Results

In all, 74 patients completed the study procedures. The demographic data for all patients are given in Table 1. There were 66 patients (89%) with invasive tumors, 60 of which were ductal carcinoma and six lobar carcinoma. Eight patients (11%) had non-invasive ductal carcinoma.

All primary tumors were identified on ^{18}F-FDG PET/CT and ^{11}C-choline PET/CT (Fig. 1). The SUV_{max} of ^{11}C-choline PET/CT was significantly lower than that of ^{18}F-FDG PET/CT ($P = 0.002$; Table 2). Conversely, the TBR of ^{11}C-choline PET/CT was significantly higher than that of ^{18}F-FDG PET/CT ($P < 0.0001$; Table 2). Using ^{18}F-FDG PET/CT, focal uptake of the primary tumor with ($n = 38$ [51%]; Fig. 2) or without ($n = 36$ [49%]) diffuse background breast uptake was demonstrated. Conversely, ^{11}C-choline PET/CT showed only focal uptake of the primary tumor in all patients. There were

Table 1. Patient demographics

Age (years)	54 ± 13 (24–78)
Tumor side	
Right	44 (59)
Left	30 (41)
Tumor size (cm)	5.9 ± 3.2 (1.8–12.0)
Main location	
Medial upper quadrant	8 (11)
Medial lower quadrant	8 (11)
Lateral upper quadrant	46 (62)
Lateral lower quadrant	6 (8)
Central	2 (3)
Invasive tumor	66 (89)
Non-invasive tumor	8 (11)

Data are given as the mean ± SD, with the range in parentheses, or as the number of patients in each group with percentages in parentheses.

doi: 10.1111/j.1349-7006.2012.02348.x
© 2012 Japanese Cancer Association

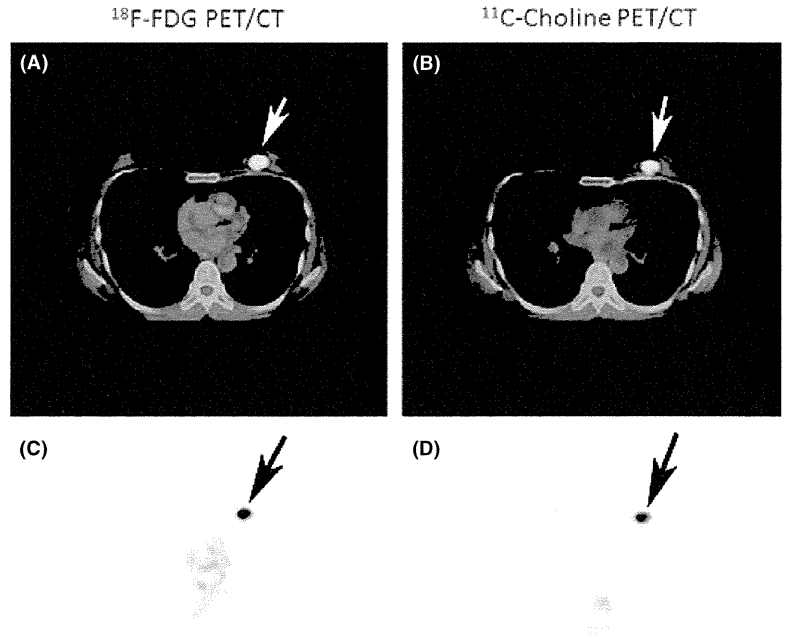

Fig. 1. Results for a 51-year-old woman with invasive ductal carcinoma of the left breast. (a,c) ^{18}F-fludeoxyglucose (FDG) PET/computed tomography (CT) images (fusion image: a; PET alone: (c) reveal a focal hypermetabolic focus in the primary tumor (arrows). The maximum standardized uptake value (SUV_{max}) was 5.5 and the tumor-to-background ratio (TBR) was 47.0. (b,d) Transverse ^{11}C-choline PET/CT images (fusion image: b; PET alone: d) also reveal a focal hypermetabolic focus in the primary tumor (arrows). The SUV_{max} was 5.0 and the TBR was 137.5. On microscopy, the tumor contained 100% invasive component.

Table 2. Computed tomography (CT)/PET measurements and pathologic components with or without diffuse background breast uptake on ^{18}F-fludeoxyglucose PET/CT

	Total	With diffuse uptake	Without diffuse uptake	*P*-value
^{11}C-Choline uptake of tumor				
SUV_{max} (g/mL)	3.7 ± 2.9	3.6 ± 3.5	3.8 ± 2.0	0.789
TBR	8.0 ± 6.0	7.7 ± 9.9	8.3 ± 9.8	0.709
^{18}F-FDG uptake of tumor				
SUV_{max} (g/mL)	4.4 ± 3.1	4.6 ± 3.6	4.2 ± 2.5	0.571
TBR	3.7 ± 2.7	3.2 ± 2.4	4.5 ± 2.9	0.016
Diameter of invasive tumor (cm)	4.1 ± 3.5	4.2 ± 4.0	4.0 ± 3.0	0.800
Diameter of non-invasive tumor (cm)	1.8 ± 2.3	2.6 ± 2.9	0.9 ± 1.0	0.002
% Invasive component	66.0 ± 36.5	54.0 ± 41.4	78.6 ± 25.4	0.003

FDG, fludeoxyglucose; SUV_{max}, maximum standardized uptake value; TBR, tumor-to-background ratio.

significant differences between patients with or without diffuse background breast uptake on ^{18}F-FDG PET/CT for TBR of ^{18}F-FDG (Table 2). There was no interaction between ^{11}C-choline uptake and background breast uptake patterns on ^{18}F-FDG PET/CT. There were significant differences for the diameter of the non-invasive component and the percentage invasive component between patients with and without diffuse background breast uptake on ^{18}F-FDG PET/CT (Table 2).

The pathologic findings and background breast uptake patterns on ^{18}F-FDG PET/CT are listed in Table 3. Patients with diffuse background breast uptake had significantly different values for percentage invasive component, FCC, necrosis, and triple negative tumor compared with patients without diffuse background breast uptake. There were no significant differences between the two groups in histologic grade, nuclear grade, structural grade, nuclear atypia, mitosis, fat invasion, or cutaneous invasion. Nor were there any significant differences in hormone receptor status between the two groups, specifically HER-2/neu, ER, and progesterone receptors. Only FCC showed an independent association with diffuse background breast uptake on multiple logistic regression analysis (OR 8.57; 95% CI 2.86–25.66; $P < 0.0001$).

There was a modest correlation between the diameter of the invasive tumor and SUV_{max} ($P < 0.0001$) or TBR ($P = 0.006$) on ^{18}F-FDG PET/CT (Table 4). Similar trends were found between the diameter of the invasive tumor and SUV_{max} ($P < 0.0001$) and TBR ($P < 0.0001$) on ^{11}C-choline PET/CT (Table 5). The TBR on ^{11}C-choline PET/CT also showed a modest correlation with the percentage invasive component ($P = 0.047$). The diameter of the non-invasive tumor was not correlated with SUV_{max} or TBR on either ^{18}F-FDG or ^{11}C-choline PET/CT.

Pathologic characteristics and tracer uptake are summarized in Table 6. Tumors with a higher histologic grade, nuclear grade, structural grade, nuclear atypia, and mitosis showed significantly higher SUV_{max} and TBR for both ^{18}F-FDG and ^{11}C-choline PET/CT. Tumors without expression of hormone receptors, including ER and progesterone receptors, and triple negative tumors showed significantly higher SUV_{max} and TBR for both ^{18}F-FDG and ^{11}C-choline PET/CT. Tumors expressing FCC and fat invasion were more likely to have high SUV_{max} and TBR on ^{11}C-choline PET/CT, but these differences were not identified in the TBR of ^{18}F-FDG PET/CT. In addition, tumors with necrosis and cutaneous invasion were found to have greater SUV_{max} and TBR only on ^{11}C-choline PET/CT. There was no significant association between the SUV_{max} or TBR and the percentage of invasive component or the HER-2/neu status for both tracers. After adjusting for age and tumor size, multiple logistic regression analysis revealed that the degree of mitosis was independently associated with high

© 2012 Japanese Cancer Association

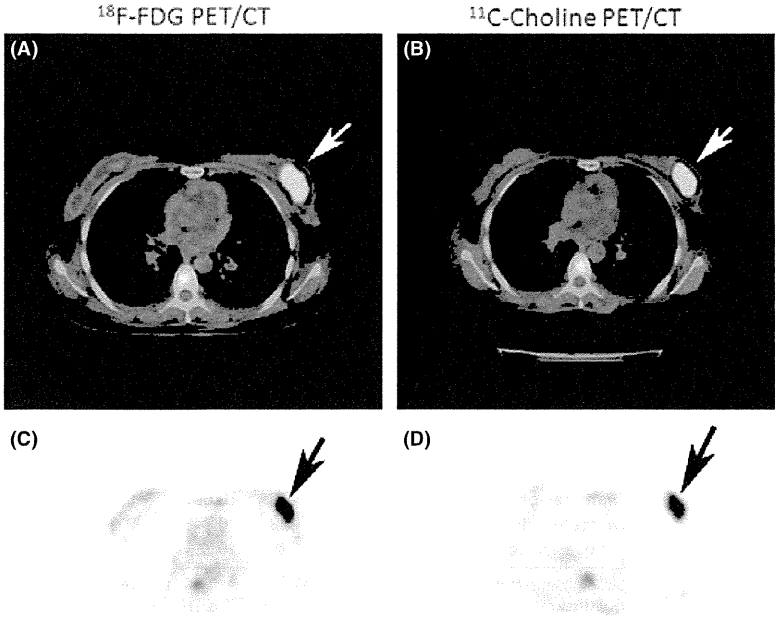

Fig. 2. Results for a 47-year-old woman with invasive scirrhous carcinoma of the left breast. (a,c) ^{18}F-fludeoxyglucose (FDG) PET/computed tomography (CT) images (fusion image: a; PET alone: c) reveal a focal hypermetabolic focus (arrows) of the primary tumor with diffuse background breast uptake. The maximum standardized uptake value (SUV_{max}) was 5.4 and the tumor-to-background ratio (TBR) was 35.7. (b,d) Transverse ^{11}C-choline PET/CT images (fusion image: b; PET alone: (d) reveal only a focal hypermetabolic focus in the primary tumor (arrows). The SUV_{max} was 5.0 and the TBR was 125.0. On microscopy, the tumor contained 15% invasive component. Diffuse fibrocystic changes were found in the background breast.

SUV_{max} (OR 7.45; 95% CI 2.21–25.11; P = 0.001) and high TBR (OR 5.41; 95% CI; 1.13–25.96; P = 0.035) of ^{11}C-choline PET/CT.

Discussion

The present study examined the association between dual-tracer uptake and histological background in breast cancer. Despite positive correlations for SUV_{max} or TBR with ^{18}F-FDG and ^{11}C-choline, mitosis was found to be correlated with ^{11}C-choline uptake only, which reflects tumor aggressiveness reported in the previous study of patients with breast cancer.[19] The results also reveal that diffuse background breast uptake on ^{18}F-FDG PET/CT depends on FCC and this pattern of uptake was not identified in any patients on ^{11}C-choline PET/CT. Our findings suggest that ^{11}C-choline may be feasible for the imaging of breast cancer particularly for patients with underlying FCC in whom mammography and ^{18}F-FDG PET/CT are limited.

Our observation of a positive correlation between mitosis and ^{11}C-choline uptake supports results reported in previous studies.[13,19] This phenomenon was not affected by the underlying histological background because comparative correlation coefficients of SUV_{max} and TBR were similar on ^{11}C-choline PET/CT. Furthermore, the association between mitosis and ^{18}F-FDG uptake was not observed, regardless of positive correlation between ^{18}F-FDG and ^{11}C-choline uptake. This discrepancy in terms of mitosis and tracer uptake in our patients is presumably caused by differences in the degree of tracer uptake.

The present study demonstrated that there were significant differences in the diameter of the non-invasive component and the percentage invasive component between patients with and without diffuse background breast uptake on ^{18}F-FDG PET/CT. However, the SUV_{max} and TBR of both tracers were similar between patients with or without diffuse background breast uptake on ^{18}F-FDG PET/CT. These results suggest that the non-invasive component of breast cancer, which refers to the DCIS component in the present study, cannot be depicted by both tracers. These findings are consistent with that of another study that suggested DCIS could not be precisely visualized by PET.[1] Neubauer *et al.*[20] suggested that the DCIS component could be detected by dynamic contrast-enhanced MRI, but the specificity was unfavorable because of an overlap in kinetic curve appearance. A major limitation of previous studies, as well as the present study, is that whole-body PET/CT scanners were used to evaluate primary lesion of the breast.

Fibrocystic changes are the most common diffuse benign condition of the breast related to changes in responses to estrogen and progesterone. The histology of FCC varies considerably and includes cysts, apocrine metaplasia, fibrosis, calcification, ductal hyperplasia, adenosis, and fibroadenomatous changes.[21,22] Because of its diverse appearances and kinetic features, FCC is major cause of false-positive findings on MRI.[23–25] As for PET studies, Yutani *et al.*[26] have previously explored the ^{18}F-FDG uptake of FCC in 38 patients with breast cancer, providing evidence that diffuse ^{18}F-FDG uptake caused by accompanying FCC obscures uptake by the primary tumor. Palmedo *et al.*[27] have confirmed that FCC is a major cause of reduced specificity in the detection of primary breast cancers on ^{18}F-FDG PET. Furthermore, Kole *et al.*[28] compared the detectability of primary lesions between ^{18}F-FDG PET and ^{11}C-tyrosine PET in patients with breast cancer and concluded that the visual assessment and delineation of the primary tumor were complicated only on ^{18}F-FDG PET when the contralateral breast tissue served as the control because FCC is a bilateral disease. As far as we were aware, the present study is the first that has been designed to evaluate the primary lesion of breast cancer using the dual tracers of ^{18}FDG and ^{11}C-choline. However, considering the high incidence of FCC, PET tracers including ^{11}C-tyrosine and ^{11}C-choline in addition to ^{18}F-FDG are more likely to fulfill specificity expectations.

The exact mechanism of ^{11}C-choline uptake by tumor cells is largely unknown; however, ^{11}C-choline has been proposed as a marker of the extracellular receptor kinase/MAPK pathway, exhibits significant uptake in tumor tissues, and is regarded as a favorable tracer for breast cancer.[13] ^{11}C-Choline uptake may occur via a choline-specific transporter protein that is overexpressed in the cell membranes of breast cancer. ^{11}C-Choline is phosphorylated by choline kinase, which is upregulated in tumor cells for the synthesis of phosphatidylcholine, and is retained within tumor cells.[11,12] Phosphatidylcholine is an essential

doi: 10.1111/j.1349-7006.2012.02348.x
© 2012 Japanese Cancer Association

Table 3. Pathologic characteristics and background breast uptake on ^{18}F-fludeoxyglucose PET/computed tomography

	No. patients		*P*-value
	With diffuse uptake	Without diffuse uptake	
Invasive component			
>30%	20	32	0.001
<30%	18	4	
Fibrocystic change			
Present	24	6	<0.0001
Absent	14	30	
Histologic grade			
1 or 2	16	22	0.102
3	22	14	
Nuclear grade			
1 or 2	16	22	0.102
3	22	14	
Structural grade			
1 or 2	14	18	0.253
3	24	18	
Nuclear atypia			
1 or 2	16	20	0.247
3	22	16	
Mitosis			
1 or 2	26	20	0.254
3	12	16	
Necrosis			
Present	22	8	0.002
Absent	16	28	
Fat invasion			
Present	22	24	0.437
Absent	16	12	
Cutaneous invasion			
Present	4	4	0.163
Absent	32	32	
HER-2/neu receptor			
Positive	22	14	0.102
Negative	16	22	
Estrogen receptor			
Positive	28	21	0.163
Negative	10	15	
Progesterone receptor			
Positive	28	21	0.163
Negative	10	15	
Triple negative			
Yes	4	11	0.032
No	34	25	

Table 4. Relationship between ^{18}F-fludeoxyglucose uptake and invasive or non-invasive tumor components

	^{18}F-FDG			
	SUV_{max}	*P*-value	TBR	*P*-value
Diameter of invasive tumor	0.381	<0.0001	0.318	0.006
Diameter of non-invasive tumor	−0.058	0.625	−0.14	0.234
% Invasive component	0.126	0.286	0.189	0.089

FDG, fludeoxyglucose; SUV_{max}, maximum standardized uptake value; TBR, tumor-to-background ratio.

Table 5. Relationship between ^{11}C-choline uptake and invasive or non-invasive tumor components

	^{11}C-Choline			
	SUV_{max}	*P*-value	TBR	*P*-value
Diameter of invasive tumor	0.425	<0.0001	0.537	<0.0001
Diameter of non-invasive tumor	0.038	0.745	−0.066	0.575
% Invasive component	0.125	0.29	0.232	0.047

SUV_{max}, maximum standardized uptake value; TBR, tumor-to-background ratio.

component of cell membranes and is involved in the modulation of transmembrane signaling by carcinogenesis. Therefore, ^{11}C-choline metabolism is accelerated in cell proliferation and is enhanced with increasing tumor grade of breast cancer. In the present study, tumors with higher histologic grade, nuclear grade, structural grade, nuclear atypia, and mitosis showed significantly higher SUV_{max} and TBR for ^{11}C-choline PET/CT. These results are in accord with those of previous *in vivo* and *in vitro* studies.[19,29]

^{11}C-Choline PET/CT has been introduced as feasible method for the evaluation of breast cancer. In the present study, tumors without ER or progesterone receptors and triple negative tumors showed greater uptake of ^{11}C-choline compared with control groups. This suggests that ^{11}C-choline uptake reflects tumor aggressiveness. In a study of 32 patients with pathologically proven breast cancer expressing ER, no association was found between ^{11}C-choline uptake and hormone receptor status.[19] The apparent discrepancy between the present study and those of the previous study[19] may be due, in large part, to differences in the patient populations studied.

In the present study, tumors exhibiting fat invasion were more likely to have a high SUV_{max} and TBR on ^{11}C-choline PET/CT, but these differences were not identified in the TBR of ^{18}F-FDG PET/CT. This appeared to be associated with diffuse ^{18}FDG uptake of breast caused by accompanying FCC, which may obscure tumor delineation. The presence of necrosis or cutaneous invasion was also found to have an association with SUV_{max} and TBR on ^{11}C-choline PET/CT. Overall, our results are consistent with those reported in *in vivo* and *in vitro* studies, in which ^{11}C-choline uptake was found to reflect tumor aggressiveness of breast cancer.[13,19]

The present study design had limitations. First, the present study was designed to assess tumor uptake of dual tracers prior to surgery. The results from a breast cancer patient population of will not fully explain the detectability of advanced or recurrent disease. Second, the present study was an observational study and not a clinical trial, which raises the possibility of confounding factors affecting the results. Third, although ^{11}C-choline is clearly a possible PET tracer for tumor localization in patients with breast cancer, its short half-life restricts its practical application. However, ^{18}F-choline is a tracer with a longer half-life than that of ^{11}C-choline, and so ^{18}F-choline may improve the accuracy of tumor localization. Additional comparative studies regarding detectability and pathologic correlation are needed to validate the findings of the present study. Although we found that ^{11}C-choline uptake reflected tumor aggressiveness in patients with breast cancer, we did not have any data regarding nodal status and follow-up management of the patients. Further studies are needed to clarify the relationship between ^{11}C-choline uptake and patient outcome with a long follow-up period.

In conclusion, the results of the present study suggest that ^{11}C-choline PET/CT allows for the evaluation of tumor aggressiveness and improves delineation of primary tumors compared with ^{18}F-FDG PET/CT in patients with breast cancer. The results demonstrate the advantages and potential of ^{11}C-choline, but clinical evaluation with a long follow-up

© 2012 Japanese Cancer Association

Table 6. Pathologic characteristics and tracer uptake

	^{11}C-Choline				^{18}F-FDG			
	SUV_{max}	*P*-value	TBR	*P*-value	SUV_{max}	*P*-value	TBR	*P*-value
% Invasive component		0.979		0.432		0.934		0.79
>30%	3.7 ± 2.3		8.5 ± 5.6		4.4 ± 3.1		3.9 ± 2.4	
<30%	3.7 ± 3.5		7.4 ± 6.4		4.4 ± 3.1		4.1 ± 3.2	
Fibrocystic change		<0.0001		<0.0001		0.002		0.429
Present	5.4 ± 3.5		11.4 ± 6.7		5.7 ± 3.5		4.3 ± 2.2	
Absent	2.5 ± 1.6		5.7 ± 4.0		3.5 ± 2.5		3.8 ± 3.1	
Histologic grade		<0.0001		<0.0001		<0.0001		<0.0001
1 or 2	2.2 ± 1.1		4.4 ± 2.5		2.9 ± 2.0		2.9 ± 2.3	
3	5.3 ± 3.3		11.8 ± 6.2		6.1 ± 3.3		5.2 ± 2.8	
Nuclear grade		<0.0001		<0.0001		<0.0001		<0.0001
1 or 2	2.2 ± 1.1		4.4 ± 2.5		2.9 ± 2.0		2.9 ± 2.3	
3	5.3 ± 3.3		11.8 ± 6.2		6.1 ± 3.3		5.2 ± 2.8	
Structural grade		<0.0001		<0.0001		<0.0001		0.011
1 or 2	2.3 ± 1.5		4.7 ± 3.5		3.0 ± 2.4		3.1 ± 2.7	
3	4.8 ± 3.2		10.5 ± 6.3		5.5 ± 3.2		4.7 ± 2.7	
Nuclear atypia		<0.0001		<0.0001		<0.0001		0.012
1 or 2	2.1 ± 1.1		4.2 ± 2.4		2.8 ± 2.0		2.8 ± 2.3	
3	5.2 ± 3.3		11.6 ± 6.1		5.9 ± 3.2		5.1 ± 2.7	
Mitosis		<0.0001		<0.0001		<0.0001		<0.0001
1 or 2	2.1 ± 1.1		4.5 ± 2.5		2.8 ± 1.8		2.6 ± 2.1	
3	6.4 ± 3.0		13.8 ± 5.5		7.1 ± 3.0		6.3 ± 2.1	
Necrosis		0.046		0.001		0.051		0.529
Present	4.5 ± 3.2		10.6 ± 7.1		5.3 ± 3.3		4.2 ± 2.6	
Absent	3.1 ± 2.6		6.2 ± 4.3		3.8 ± 2.9		3.8 ± 2.9	
Fat invasion		0.003		0.002		0.024		0.061
Present	4.5 ± 3.3		9.6 ± 6.5		5.0 ± 3.4		4.4 ± 2.8	
Absent	2.4 ± 1.5		5.3 ± 3.6		3.4 ± 2.2		3.2 ± 2.6	
Cutaneous invasion		0.004		<0.0001		0.133		0.706
Present	6.4 ± 3.1		14.8 ± 7.3		6.0 ± 4.7		4.3 ± 2.2	
Absent	3.4 ± 2.7		7.2 ± 5.3		4.2 ± 2.8		3.9 ± 2.8	
HER-2/neu receptor		0.53		0.772		0.518		0.766
Positive	3.5 ± 2.6		8.2 ± 6.0		4.2 ± 2.7		4.1 ± 3.1	
Negative	3.9 ± 3.2		7.8 ± 6.0		4.7 ± 3.5		3.9 ± 2.5	
Estrogen receptor		<0.0001		<0.0001		<0.0001		<0.0001
Positive	2.3 ± 1.4		5.4 ± 3.4		3.1 ± 1.8		2.9 ± 2.9	
Negative	6.3 ± 3.3		13.1 ± 6.6		7.0 ± 3.5		6.1 ± 2.5	
Progesterone receptor		<0.0001		<0.0001		<0.0001		<0.0001
Positive	2.4 ± 1.5		5.6 ± 3.7		3.1 ± 1.9		2.9 ± 2.9	
Negative	6.2 ± 3.4		12.7 ± 6.8		7.0 ± 3.5		6.1 ± 2.5	
Triple negative		<0.001		<0.0001		<0.0001		0.002
Yes	6.7 ± 3.3		12.9 ± 6.5		7.4 ± 3.8		6.2 ± 2.1	
No	2.9 ± 2.2		6.7 ± 5.2		3.7 ± 2.4		3.4 ± 2.7	

FDG, fludeoxyglucose; SUV_{max}, maximum standardized uptake value; TBR, tumor-to-background ratio.

period is warranted to clarify the exact role of this technique and how it affects patient outcome.

Acknowledgments

This work was supported, in part, by a Grant-in-Aid for Cancer Research (21–5-2) from the Ministry of Health, Labour and Welfare of Japan.

Disclosure Statement

The authors declare that they have no conflicts of interest.

Abbreviations

CT	computed tomography
DCIS	ductal carcinoma *in situ*
ER	estrogen receptor
FCC	fibrocystic change
^{18}F-FDG2-[^{18}F]	fluoro-2-deoxy-D-glucose
HER-2/neu	human epidermal growth factor-2
MAPK	mitogen-activated protein kinase
SUV_{max}	maximum standardized uptake value
TBR	tumor-to-background ratio

References

1 Nieweg OE, Kim EE, Wong WH *et al.* Positron emission tomography with fluorine-18-deoxyglucose in the detection and staging of breast cancer. *Cancer* 1993; **71**: 3920–5.

2 Rosen EL, Eubank WB, Mankoff DA. FDG PET, PET/CT, and breast cancer imaging. *Radiographics* 2007; **27**: S215–29.

3 Mahner S, Schirrmacher S, Brenner W *et al.* Comparison between positron emission tomography using 2-[fluorine-18]fluoro-2-deoxy-D-glucose, conven-

doi: 10.1111/j.1349-7006.2012.02348.x
© 2012 Japanese Cancer Association

tional imaging and computed tomography for staging of breast cancer. *Ann Oncol* 2008; **19**: 1249–54.
4 Tatsumi M, Cohade C, Mourtzikos KA, Fishman EK, Wahl RL. Initial experience with FDG-PET/CT in the evaluation of breast cancer. *Eur J Nucl Med Mol Imaging* 2006; **33**: 254–62.
5 Lim HS, Yoon W, Chung TW *et al.* FDG PET/CT for the detection and evaluation of breast diseases: usefulness and limitations. *Radiographics* 2007; **27**: S197–213.
6 Pisano ED, Johnston RE, Chapman D *et al.* Human breast cancer specimens: diffraction-enhanced imaging with histologic correlation. Improved conspicuity of lesion detail compared with digital radiography. *Radiology* 2000; **214**: 895–901.
7 Venta LA, Wiley EL, Gabriel H, Adler YT. Imaging features of focal breast fibrosis: mammographic–pathologic correlation of noncalcified breast lesions. *AJR Am J Roentgenol* 1999; **173**: 309–16.
8 Chen JH, Liu H, Baek HM, Nalcioglu O, Su MY. Magnetic resonance imaging features of fibrocystic change of the breast. *Magn Reson Imaging* 2008; **26**: 1207–14.
9 van den Bosch MA, Daniel BL, Mariano MN *et al.* Magnetic resonance imaging characteristics of fibrocystic change of the breast. *Invest Radiol* 2005; **40**: 436–41.
10 Yutani K, Shiba E, Kusuoka H *et al.* Comparison of FDG-PET with MIBI-SPECT in the detection of breast cancer and axillary lymph node metastasis. *J Comput Assist Tomogr* 2000; **24**: 274–80.
11 Ishidate K. Choline/ethanolamine kinase from mammalian tissues. *Biochim Biophys Acta* 1997; **1348**: 70–8.
12 Uchida T, Yamashita S. Molecular cloning, characterization, and expression in *Escherichia coli* of a cDNA encoding mammalian choline kinase. *J Biol Chem* 1992; **267**: 10156–62.
13 Kenny LM, Contractor KB, Hinz R *et al.* Reproducibility of [^{11}C]choline-positron emission tomography and effect of trastuzumab. *Clin Cancer Res* 2010; **16**: 4236–45.
14 Fukukita H, Senda M, Terauchi T *et al.* Japanese guideline for the oncology FDG-PET/CT data acquisition protocol: synopsis of Version 1.0. *Ann Nucl Med* 2010; **24**: 325–34.
15 Hara T, Yuasa M. Automated synthesis of [^{11}C]choline, a positron-emitting tracer for tumor imaging. *Appl Radiat Isot* 1999; **50**: 531–3.
16 Sobin LH, Wittekind C. *UICC TNM Classification of Malignant Tumours*, 6th edn. New York: Wiley, 2002.
17 Elston CW, Ellis IO. Pathological prognostic factors in breast cancer. I. The value of histological grade in breast cancer: experience from a large study with long-term follow-up. *Histopathology* 2002; **41**: 154–61.
18 McCarty KS Jr, Szabo E, Flowers JL *et al.* Use of a monoclonal anti-estrogen receptor antibody in the immunohistochemical evaluation of human tumors. *Cancer Res* 1986; **46**: s4244–8.
19 Contractor KB, Kenny LM, Stebbing J *et al.* [^{11}C]choline positron emission tomography in estrogen receptor-positive breast cancer. *Clin Cancer Res* 2009; **15**: 5503–10.
20 Neubauer H, Li M, Kuehne-Held R, Schneider A, Kaiser WA. High grade and non-high grade ductal carcinoma *in situ* on dynamic MR mammography: characteristic findings for signal increase and morphological pattern of enhancement. *Br J Radiol* 2003; **76**: 3–12.
21 Guinebretière JM, Lê Monique G, Gavoille A, Bahi J, Contesso G. Angiogenesis and risk of breast cancer in women with fibrocystic disease. *J Natl Cancer Inst* 1994; **86**: 635–6.
22 Bodian CA, Perzin KH, Lattes R, Hoffmann P. Reproducibility and validity of pathologic classifications of benign breast disease and implications for clinical applications. *Cancer* 1993; **71**: 3908–13.
23 Revelon G, Sherman ME, Gatewood OM, Brem RF. Focal fibrosis of the breast: imaging characteristics and histopathologic correlation. *Radiology* 2000; **216**: 255–9.
24 Orel SG, Schnall MD, LiVolsi VA, Troupin RH. Suspicious breast lesions: MR imaging with radiologic–pathologic correlation. *Radiology* 1994; **190**: 485–93.
25 Fobben ES, Rubin CZ, Kalisher L, Dembner AG, Seltzer MH, Santoro EJ. Breast MR imaging with commercially available techniques: radiologic–pathologic correlation. *Radiology* 1995; **196**: 143–52.
26 Yutani K, Tatsumi M, Uehara T, Nishimura T. Effect of patients being prone during FDG PET for the diagnosis of breast cancer. *AJR Am J Roentgenol* 1999; **173**: 1337–9.
27 Palmedo H, Bender H, Grünwald F *et al.* Comparison of fluorine-18 fluorodeoxyglucose positron emission tomography and technetium-99*m* methoxyisobutylisonitrile scintimammography in the detection of breast tumours. *Eur J Nucl Med* 1997; **24**: 1138–45.
28 Kole AC, Nieweg OE, Pruim J *et al.* Standardized uptake value and quantification of metabolism for breast cancer imaging with FDG and l-[1–11C]tyrosine. *J Nucl Med* 1997; **38**: 692–6.
29 Yoshimoto M, Waki A, Obata A, Furukawa T, Yonekura Y, Fujibayashi Y. Radiolabeled choline as a proliferation marker: comparison with radiolabeled acetate. *Nucl Med Biol* 2004; **31**: 859–65.

© 2012 Japanese Cancer Association

Microbiology (2011), **157**, 2422–2432 DOI 10.1099/mic.0.048488-0

A conserved residue, PomB-F22, in the transmembrane segment of the flagellar stator complex, has a critical role in conducting ions and generating torque

Takashi Terauchi,† Hiroyuki Terashima,†‡ Seiji Kojima and Michio Homma

Correspondence
Michio Homma
g44416a@cc.nagoya-u.ac.jp

Division of Biological Science, Graduate School of Science, Nagoya University, Chikusa-Ku, Nagoya 464-8602, Japan

Bacterial flagellar motors exploit the electrochemical potential gradient of a coupling ion (H^+ or Na^+) as their energy source, and are composed of stator and rotor proteins. Sodium-driven and proton-driven motors have the stator proteins PomA and PomB or MotA and MotB, respectively, which interact with each other in their transmembrane (TM) regions to form an ion channel. The single TM region of PomB or MotB, which forms the ion-conduction pathway together with TM3 and TM4 of PomA or MotA, respectively, has a highly conserved aspartate residue that is the ion binding site and is essential for rotation. To investigate the ion conductivity and selectivity of the Na^+-driven PomA/PomB stator complex, we replaced conserved residues predicted to be near the conserved aspartate with H^+-type residues, PomA-N194Y, PomB-F22Y and/or PomB-S27T. Motility analysis revealed that the ion specificity was not changed by either of the PomB mutations. PomB-F22Y required a higher concentration of Na^+ to exhibit swimming, but this effect was suppressed by additional mutations, PomA-N194Y or PomB-S27T. Moreover, the motility of the PomB-F22Y mutant was resistant to phenamil, a specific inhibitor for the Na^+ channel. When PomB-F22 was changed to other amino acids and the effects on swimming ability were investigated, replacement with a hydrophilic residue decreased the maximum swimming speed and conferred strong resistance to phenamil. From these results, we speculate that the Na^+ flux is reduced by the PomB-F22Y mutation, and that PomB-F22 is important for the effective release of Na^+ from PomB-D24.

Received 21 January 2011
Revised 9 May 2011
Accepted 26 May 2011

INTRODUCTION

Some ion channels and transporters that exist in cell membranes can selectively translocate only a particular ion. The high ion specificity of an ion channel or transporter is extremely important for signal transduction, membrane excitability and the homeostasis of organisms. Each selective ion transporter, which is coupled to a sodium ion, such as LeuT, NtpK or NhaA, possesses an ion binding pocket. A particular ion and/or a transport substrate interacts with the ion binding pocket, induces a conformational change, and is then translocated to the opposite side across the membrane (Gouaux & Mackinnon, 2005; Yamashita *et al.*, 2005; Hunte *et al.*, 2005; Murata *et al.*, 2005, 2008). For example, in the Na^+-driven V-type ATPase of *Enterococcus hirae*, the transmembrane complex V_o, which conducts Na^+ (or Li^+), is composed of a membrane rotor ring (K-ring) comprising oligomers of NtpK and a single copy of the NtpI subunit. It has been suggested that the cavity size of the K-ring binding pocket contributes to the ion specificity, that five residues (L^{61}, T^{64}, Q^{65}, Q^{110}, E^{139}) of NtpK are involved in the Na^+ binding to the K-ring, and that the essential glutamate E^{139} is conserved in the homologous subunits of H^+-driven V-ATPase (Murata *et al.*, 2005, 2008). Bacterial flagellar motors are rotary motors which convert the electrochemical potential difference of a coupling ion (H^+ or Na^+) across the cytoplasmic membrane into torque, which rotates the flagellum. *Escherichia coli* and *Salmonella* use H^+ as the coupling ion, whereas *Vibrio* and alkaliphilic *Bacillus* use Na^+ (Kojima & Blair, 2004; Terashima *et al.*, 2008).

Each flagellar motor is composed of a stator and a rotor. The stator serves as a torque-generating unit and is thought to work by interacting with the rotor. MotA and MotB are stator proteins in the H^+-driven motor of *E. coli* and *Salmonella*, while PomA and PomB, which are orthologues

Abbreviation: TM, transmembrane.

†These authors contributed equally to this work.

‡Present address: Department of Anesthesiology, Weill Cornell Medical College, Cornell University, 1300 York Ave., New York 10065, USA.

A supplementary movie is available with the online version of this paper.

048488 © 2011 SGM *Printed in Great Britain*

of MotA and MotB, are found in the Na^+-driven motor of *Vibrio* spp. (Asai *et al.*, 1997; Dean *et al.*, 1984; Stader *et al.*, 1986). Only the Na^+-driven motor of *Vibrio* spp. requires additional motor proteins, MotX and MotY, for torque generation (Okabe *et al.*, 2001; Okunishi *et al.*, 1996). PomA and PomB (MotA and MotB) are membrane proteins and form an $A_4:B_2$ heterohexamer (Kojima & Blair, 2004; Sato & Homma, 2000a, b; Yorimitsu *et al.*, 2004). PomA (MotA) has four transmembrane (TM) segments, whereas PomB (MotB) has only a single TM segment (Asai *et al.*, 1997; Chun & Parkinson, 1988; Zhou *et al.*, 1995). The C-terminal half of PomB (MotB) associates with the peptidoglycan layer and at least 11 PomA/B (MotA/B) complexes assemble around the rotor (Kojima *et al.*, 2009; Leake *et al.*, 2006; Reid *et al.*, 2006). The coupling ion is taken through an ion-conducting pathway formed in the PomA/B (MotA/B) complex (Blair & Berg, 1990; Sato & Homma, 2000b). The ion influx induces a conformational change of the stator complex, which causes an interaction between PomA (MotA) and the rotor component FliG, and it has been inferred that the torque is generated by that interaction (Kojima & Blair, 2001; Lloyd & Blair, 1997; Yorimitsu *et al.*, 2002; Zhou & Blair, 1997; Zhou *et al.*, 1998a). The ion-conducting pathway is thought to be formed mainly by the third and fourth TM segments of PomA (MotA) and the single TM segment of PomB (MotB) (Braun & Blair, 2001; Braun *et al.*, 2004; Sudo *et al.*, 2009b; Yakushi *et al.*, 2004). PomB (MotB) has a completely conserved aspartate residue (PomB-D24 for *Vibrio*, MotB-D32 for *E. coli*) which is essential for torque generation, and is a binding site of the coupling ion (Sudo *et al.*, 2009a; Zhou *et al.*, 1998b). Recently, it has been shown that this essential aspartate residue in PomB can be transferred to the TM segment of PomA. The transferred residue of PomA-N194D, which is a mutation in TM4, is able to partially rescue the motility defect in PomB-D24N, which suggests that PomA-N194 and PomB-D24 form an Na^+ binding pocket for the coupling ion (Terashima *et al.*, 2010).

Studies using chimeric proteins between H^+-type MotA/B of *Rhodobacter sphaeroides* or *E. coli* and Na^+-type PomA/B of *Vibrio alginolyticus* suggest that the B subunit is important for determining the ion specificity of the stator complex (Asai *et al.*, 2000, 2003). In *Bacillus subtilis*, two types of stator complexes, MotA/B as the H^+ type and MotP/S as the Na^+ type, assemble around a single flagellar base, and the ion dependence of the functional hybrid stator complex (MotA/S or MotP/B) suggests the importance of the B subunit for determining the coupling ion (Ito *et al.*, 2005). It has been reported that exchanging only three amino acids between MotB and MotS in *B. subtilis* can convert the ion specificity from the H^+ type to the Na^+ type and vice versa (Terahara *et al.*, 2008). However, it remains unclear how the ion specificity is determined and how the coupling ion is coordinated by residues in the ion binding pocket, which then releases the ion from the binding pocket into the cytoplasm.

To investigate how the ion is selectively recognized in the stator complex and is released from it, we focused here on residues close to the essential aspartate residue of PomB. We constructed mutants in which the conserved residue in the Na^+-type stator was changed to the corresponding residue in the H^+-type stator, and the effects on motility were analysed. Thus we found a residue involved in determining the ion specificity and/or the ion release from PomB-D24.

METHODS

Bacterial strains, plasmids and growth conditions. The bacterial strains and plasmids used in this study are shown in Table 1. Site-directed mutagenesis of *pomA* or *pomB* was done using the QuikChange procedure (Stratagene). *V. alginolyticus* was cultured in VC broth [0.5 % (w/v) Bacto tryptone, 0.5 % (w/v) yeast extract, 0.4 % (w/v) K_2HPO_4, 3 % (w/v) NaCl, 0.2 % (w/v) glucose] or in VPG500 medium [1 % (w/v) Bacto tryptone, 0.4 % (w/v) K_2HPO_4, 500 mM NaCl, 0.5 % (w/v) glycerol] at 30 °C. *E. coli* was cultured in LB broth [1 % (w/v) Bacto tryptone, 0.5 % (w/v) yeast extract, 0.5 % (w/v) NaCl]. Chloramphenicol was added to a final concentration of 2.5 μg ml^{-1} for *V. alginolyticus* and 25 μg ml^{-1} for *E. coli*.

Swimming assay in semisolid agar. VPG500 semisolid agar [1 % (w/v) Bacto tryptone, 0.4 % (w/v) K_2HPO_4, 500 mM NaCl, 0.5 % (w/v) glycerol, 0.25 % (w/v) Bacto agar] containing 0.02 % (w/v) arabinose was used for motility assays of *V. alginolyticus*. A 1 μl aliquot of each overnight culture was spotted onto VPG500 semisolid agar containing 0.02 % (w/v) arabinose or VPG500 semisolid agar containing 0.02 % (w/v) arabinose and 200 μM phenamil, and was incubated at 30 °C for the desired time.

Introduction of plasmids into *V. alginolyticus*. Transformation of *Vibrio* cells was carried out using electroporation, as described previously (Kawagishi *et al.*, 1994).

Measurement of swimming speed for *Vibrio* cells. Overnight cultures were inoculated into VPG500 medium containing 0.02 % (w/v) arabinose at a 100-fold dilution. Cells were incubated at 30 °C for 4 h and were then collected by centrifugation at 2000 ***g*** for 5 min. Cells were resuspended in TMN (50 mM Tris/HCl, pH 7.0, 5 mM $MgCl_2$, 5 mM glucose, total ion strength 500 mM NaCl and KCl), TMN0 (Na^+ 0 mM, K^+ 500 mM), TMN5 (Na^+ 5 mM, K^+ 495 mM), TMN10 (Na^+ 10 mM, K^+ 490 mM), TMN20 (Na^+ 20 mM, K^+ 480 mM), TMN50 (Na^+ 50 mM, K^+ 450 mM), TMN100 (Na^+ 100 mM, K^+ 400 mM), TMN300 (Na^+ 300 mM, K^+ 200 mM) or TMN500 (Na^+ 500 mM, K^+ 0 mM) buffer. The suspensions were recentrifuged and then resuspended in the same TMN buffer, and cells were diluted to 1 : 50 in the same TMN buffer and kept at room temperature for 15 min. Swimming of the cells was observed using dark-field microscopy immediately after the addition of serine to a final concentration of 20 mM to make the cells swim smoothly. Swimming speeds were determined from analysis of at least 20 individual cells. To investigate the effect of phenamil on swimming, cells were suspended in TMN300 buffer and phenamil was added to a final concentration of 0, 2.5, 5, 10, 20, 50 or 100 μM. After the cells were exposed to phenamil for 15 s, swimming cells were recorded and then measured by using software for motion analysis (Move-tr/2D; Library Co.).

Immunoblotting. Cells were resuspended in SDS loading buffer and boiled at 95 °C for 5 min, and then were subjected to SDS-PAGE and immunoblotting as described previously (Yorimitsu *et al.*, 1999). The

Table 1. Bacterial strains and plasmids used in the study

Abbreviations: Mot$^-$, non-motile; Cm^r, chloramphenicol resistant; P_{BAD}, *araBAD* promoter.

Strain or plasmid	Genotype or description	Reference
***V. alginolyticus* strains**		
NMB191	VIO5 *pomAB* (Mot$^-$)	Yorimitsu *et al.* (1999)
sp2	NMB191, up-motile phenotype when PomAB is expressed	Terashima *et al.* (2010)
***E. coli* strain**		
JM109	*recA1 endA1 gyrA96 thi hsdR17 supE44 relA1* λ^- Δ(*lac-proAB*) (F′ *traD36 proAB lacI*^{q} *lacZ*ΔM15)	Yanisch-Perron *et al.* (1985)
Plasmids		
pBAD33	Cm^r P_{BAD}	Guzman *et al.* (1995)
pHFAB	*pomA* and *pomB* in pBAD33	Fukuoka *et al.* (2005)

antibody to PomA (PomA1312) has been reported previously (Yorimitsu *et al.*, 1999) and the antibody to PomB ($PomB_{C2}$B0455) was prepared as follows: an N-terminally truncated PomB variant consisting of residues 59–315 ($PomB_{C2}$) with a His_6-tag fused at its C terminus was constructed, and was overexpressed in BL21(DE3) cells from plasmid pTSK36, a derivative of pET22b. Cells were disrupted and a soluble fraction was isolated by ultracentrifugation. His-tagged $PomB_{C2}$ was purified from this soluble fraction by using a HisTrap column followed by a HiTrap Q column (GE Healthcare). Purified $PomB_{C2}$ was separated by SDS-PAGE, stained with Coomassie blue R250 and excised for immunization. The rabbit anti-$PomB_{C2}$ antibody ($PomB_{C2}$B0455) was produced by Biogate Co. Horseradish peroxidase-linked goat anti-rabbit IgG (Santa Cruz) was used as the secondary antibody.

RESULTS

Motility of cells producing PomB-L35V/S38A/E41S or PomB-L35V in Na^+-free buffer

MotA/B and MotP/S of *B. subtilis* are the stators for the H^+- and Na^+-driven motors, respectively. When conserved residues in the H^+- or Na^+-type motors were exchanged between MotB and MotS (MotB-V35L + A38S + S41Q or MotS-L41V + S44A + Q47S), MotA/B was converted to the Na^+-driven type, whereas MotP/S was converted to the H^+-driven type (Terahara *et al.*, 2008). Therefore, we substituted the corresponding residues of the Na^+-type *Vibrio* PomB with those of the H^+-type *E. coli* MotB (PomB-L35V + S38A + E41S or PomB-L35V) (Fig. 1). The swimming speeds of cells producing PomB-L35V or PomB-L35V + S38A + E41S were measured in buffer containing 0–300 mM NaCl (Fig. 2). The maximum swimming speed of cells producing PomB-L35V decreased to approximately 85 % of the wild-type value. The maximum swimming speed of cells producing PomB-L35V + S38A + E41S decreased to approximately 50 % of the wild-type value. However, in sodium-free buffer, cells producing PomB-L35V + S38A + E41S or PomB-L35V were not able to swim, and the swimming speed profiles were dependent on Na^+ concentration (Fig. 2).

Motility of mutants converted from an Na^+- to an H^+-type residue

To investigate further the mechanism of the ion translocation and specificity in the stator complex, we focused on the residues that are conserved in the TM segments of the Na^+-type stator proteins but not in those of the H^+-type proteins, or on some residues around the boundary of the TM segments, because they may function as the entrance for ion conductance. We targeted the residues PomA-N194, PomB-F22 and PomB-S27, and replaced them with the corresponding amino acid of the H^+-type protein (PomA-N194Y, PomB-F22Y and PomB-S27T) (Fig. 1). The swimming speeds of cells expressing PomA-N194Y, PomB-F22Y and PomB-S27T were measured in buffer containing 0–500 mM NaCl (Fig. 3). All mutants were able to swim in the presence of NaCl but not in Na^+-free buffer, suggesting that the ion specificity was not converted. The maximum swimming speed of cells producing PomA-N194Y decreased to approximately 50 % of the wild-type value. The maximum swimming speed of cells producing PomB-F22Y was almost the same as that of the wild-type; however, these cells were unable to swim in the presence of 5 mM NaCl and appeared to have a swimming threshold between 5 and 10 mM NaCl (Fig. 3b). The swimming speed of cells expressing PomB-S27T decreased to approximately 60 % of the wild-type value. The amount of each mutant protein expressed from the plasmid was not affected by any of the mutations (data not shown).

To investigate whether the phenotype is affected by combinations of the mutations, mutants producing PomA-N194Y/PomB-F22Y, PomB-F22Y + S27T and PomB-F22Y + L35V were constructed, and their swimming speeds were measured at 0–50 mM NaCl (Fig. 4). These combination mutants were not able to swim in Na^+-free buffer, suggesting that their ion specificity was not converted. Production of PomA-N194Y/PomB-F22Y and PomB-F22Y + S27T conferred swimming ability in buffer containing 5 mM Na^+, but PomB-F22Y + L35V did not, indicating that PomA-N194Y and PomB-S27T suppressed the threshold phenotype of PomB-F22Y. Cells producing PomB-F22Y + L35V

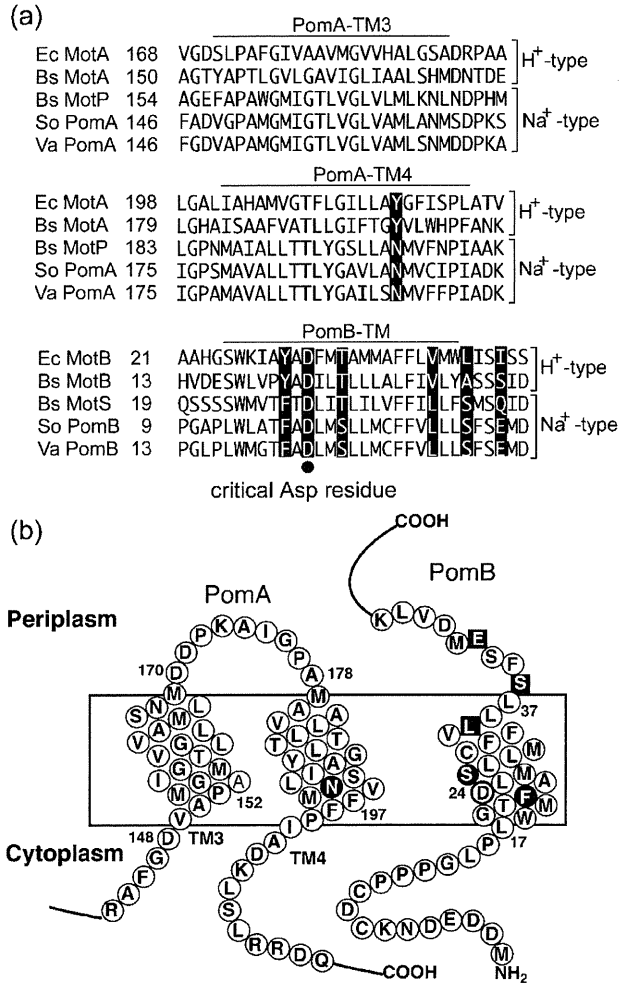

Fig. 1. (a) Amino acid sequence alignments of TM3 and TM4 of PomA and the TM of PomB for various species. White letters on a black background show conserved residues which are predicted to be around the conserved aspartate and residues that were replaced in the triple mutant. The highly conserved Asp residue is marked with a filled circle. Ec, *E. coli*; Bs, *B. subtilis*; So, *Shewanella oneidensis*; Va, *V. alginolyticus*. (b) Putative membrane topology of TM3 and TM4 of PomA and the TM of PomB, and sites of residue substitutions made in this study. The bold circle shows the essential Asp of PomB (Asp24). White letters in filled squares show residues that were replaced in the triple mutant (PomB-L35 and S38, E41). White letters in filled circles show the conserved residues which are predicted to be around the conserved Asp and which replaced the H^+-type residue in this study.

required an Na^+ concentration between 10 and 20 mM NaCl to exhibit swimming.

Motility of various PomB-F22 mutants

The phenotype of the PomB-F22Y mutant suggested that the mutation may affect ion conduction or torque

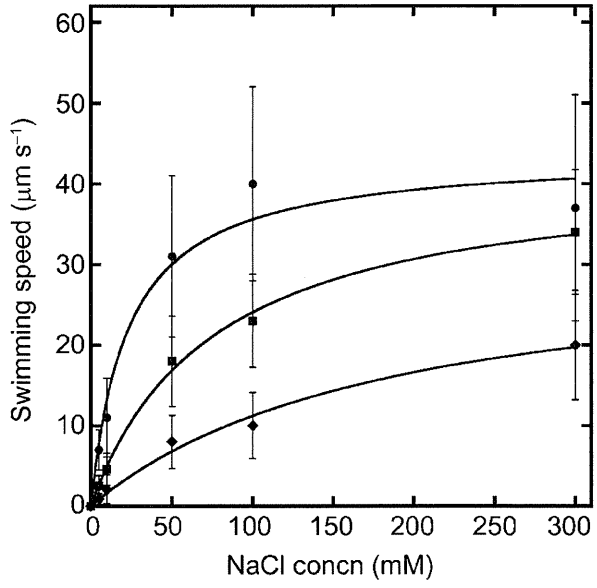

Fig. 2. Swimming speeds of cells producing PomA/PomB (●), PomA/PomB-L35V+S38A+E41S (◆) or PomA/PomB-L35V (■). Overnight cultures of cells were inoculated in VPG500 medium and incubated at 30 °C for 4 h. Swimming speeds were measured in buffer containing 0–300 mM NaCl.

generation. We carried out site-directed mutagenesis to replace Phe22 of PomB with various amino acid residues, K, D, L, W, Y, A, S and N. The swimming speed for each mutant was then measured in buffer containing 0–500 mM Na^+ (data not shown). Except for the F22K and F22D mutants, the other six mutants exhibited motility at 500 mM NaCl. F22L and F22W showed nearly the same Na^+ dependence and swimming speed as the wild-type. On the other hand, F22A had an Na^+ threshold to exhibit swimming between 5 and 10 mM NaCl, similar to F22Y (Fig. 5a), and F22S and F22N had a threshold between 10 and 20 mM NaCl (Fig. 5b, c). The maximum swimming speeds of the F22L, F22W and F22Y mutants were almost the same as the original F22, while that of the F22A, F22S and F22N mutants decreased by approximately 50 % compared with F22. We also checked the swimming ability of the PomB-F22 mutants in semisolid agar containing 500 mM NaCl (Fig. 6a). Except for the F22L mutant, the swimming abilities in liquid and in semisolid agar for each mutant were comparable. The swimming ring size of F22L decreased to approximately 50 % of the wild-type value. These results show that various mutations of the F22 residue of PomB seem to affect motility in an Na^+ concentration-dependent manner. Small hydrophobic (F22A) or hydrophilic (F22S and F22N, F22Y) residues showed a threshold of Na^+ concentration to exhibit swimming (Fig. 5). However, large hydrophobic residues (F22L and F22W) did not show such a threshold (data not shown). The side-chain volume of Leu and Asn is

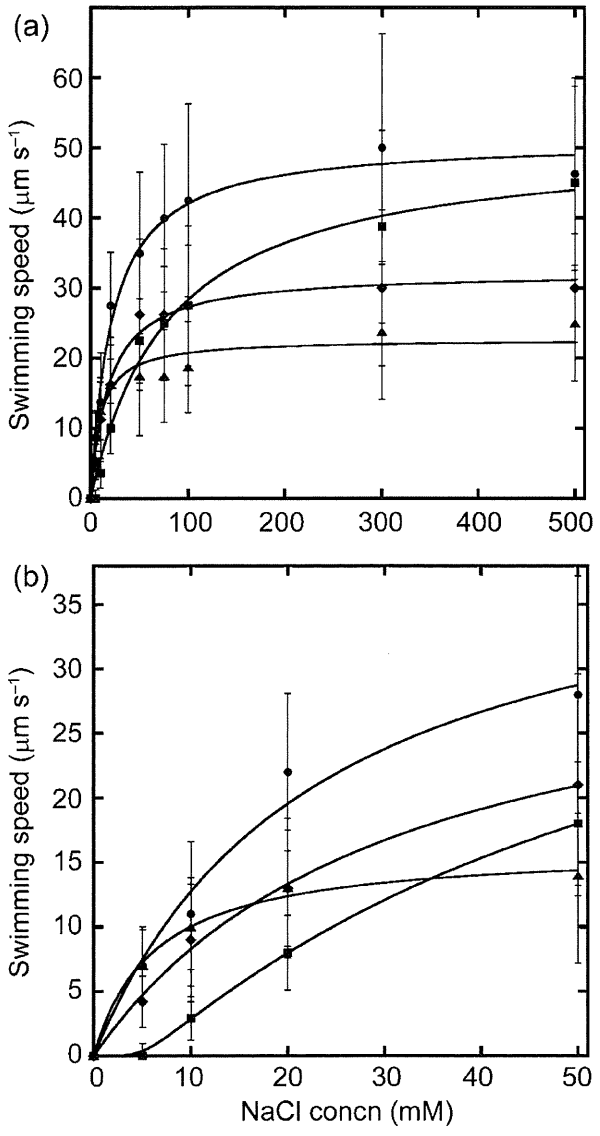

Fig. 3. Swimming speeds of cells producing PomA/PomB (●), PomA-N194Y/PomB (▲), PomA/PomB-F22Y (■) or PomA/PomB-S27T (◆). (a) Swimming speeds were measured as described in the legend of Fig. 2. (b) Enlargement of the swimming speed data between 0 and 50 mM shown in (a).

almost the same; however, the substitutions conferred different phenotypes. Thus, the hydrophobicity of F22 seems to be important for stator function through ion conduction.

Phenamil resistance of various PomB-F22 mutants

If a mutation affects the Na^+-dependent swimming property, it might also change the sensitivity to an Na^+ channel blocker or a specific inhibitor of Na^+-driven motors such as phenamil. We checked the motilities of various PomB-F22 mutants in the presence of 200 μM phenamil by using semisolid agar containing 500 mM NaCl (Fig. 6b). The F22K and F22D mutants did not show swimming expansion even in the absence of phenamil. F22A showed a similar swimming expansion profile to that of the wild-type, while F22L and F22Y showed a slightly larger swimming expansion than the wild-type. F22W, F22S and F22N showed an even larger swimming expansion than F22L and F22Y. We next measured the swimming speeds of cells producing PomB-F22W, F22S, F22N and F22Y in buffer containing 300 mM Na^+ with a final concentration of 0–100 μM phenamil (Fig. 7). Mutants producing F22W or F22Y were able to swim in the presence of 100 μM phenamil, but the swimming speed of cells decreased with increasing phenamil concentration. On the other hand, the motility of cells producing F22S or F22N remained at the same level, even at higher concentrations of phenamil. F22S and F22N showed strong resistance to phenamil. These results suggest that replacement of Phe22 with a large hydrophobic (W) or hydrophilic residues (S and N, Y) weakens the interaction with phenamil.

Conversion of the ion specificity in the up-motile strain

When PomA-N194Y, PomB-F22Y or PomB-S27T was produced in the sp2 strain, which gives an increased motility phenotype (Terashima *et al.*, 2010), PomA-N194Y conferred slight swimming ability (mean ± SD 1.8 ± 0.76 μm s^{-1}) even in Na^+-free buffer (see Supplementary Movie), but the wild-type and PomB-F22Y and PomB-S27T mutants did not (data not shown). Because we suspected possible contamination with Na^+ from the VPG500 broth, we washed the cells twice with Na^+-free buffer. Cells producing PomA-N194Y conferred only slight swimming ability, even after the additional washes. In 0 mM Na^+ buffer with phenamil or carbonyl cyanide *m*-chlorophenylhydrazone (CCCP), this mutant was no longer able to confer motility. From these results, we were not able to determine which ion was used to rotate the flagellar motor by PomA-N194Y. However, the wild-type PomA/B was not able to confer motility at all by using the standard protocol with two washes. Therefore, we speculate that PomA-N194Y may use a different ion, such as H^+, to rotate the flagellar motor; alternatively, the PomA-N194 stator may be driven by an extremely low Na^+ concentration.

DISCUSSION

It has been proposed that the highly conserved aspartate residue (PomB-D24) binds the coupling ion and forms an ion binding pocket with PomA-N194 (Fig. 8) (Sudo *et al.*, 2009a; Terashima *et al.*, 2010). If the ion binding pocket is not the correct size for the coupling ion or if residues of the ion binding pocket are not correctly aligned to interact with the coupling ion, the conformational change of the

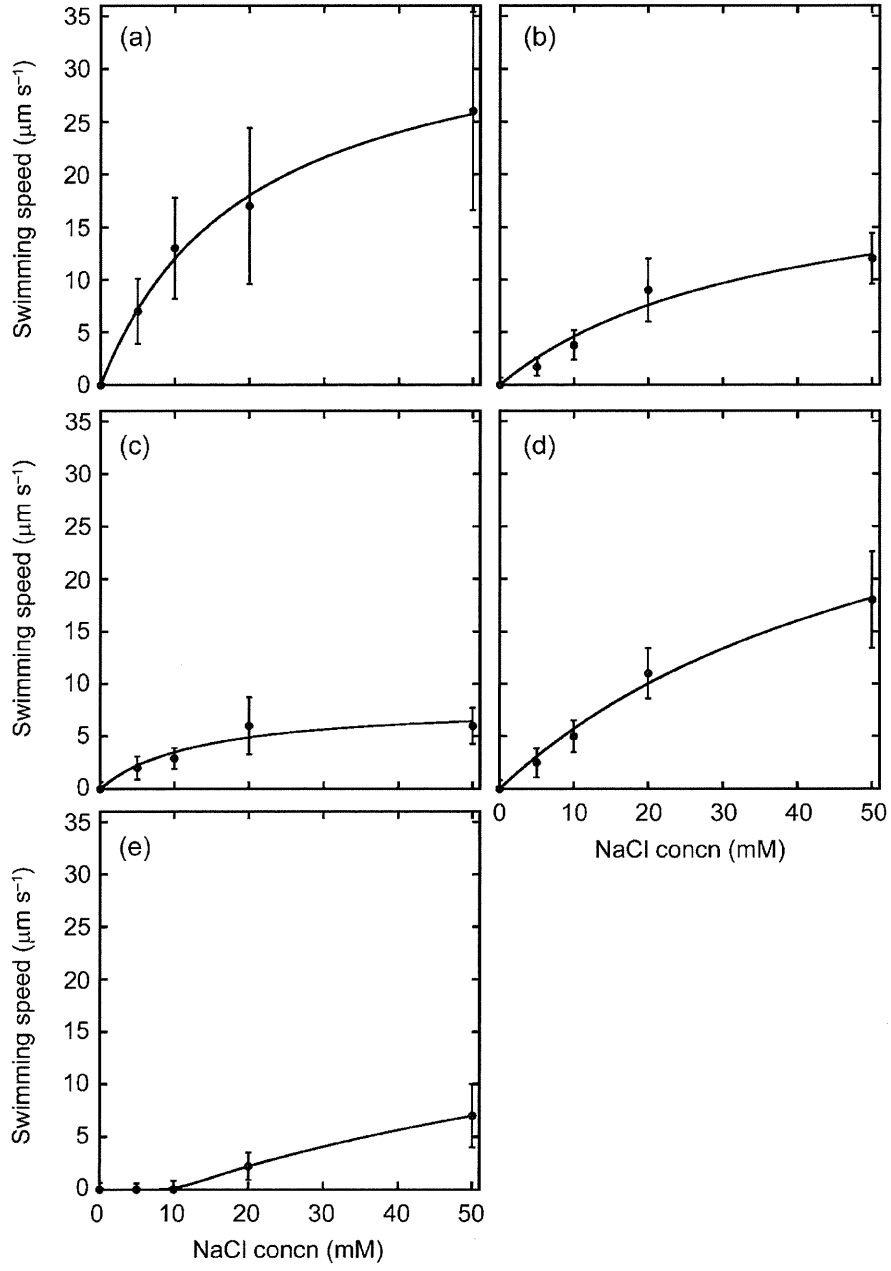

Fig. 4. Swimming speeds of the mutant stators combined with PomB-F22Y. Swimming speeds of cells producing PomA/PomB (a), PomA/PomB-L35V (b), PomA-N194Y/PomB-F22Y (c), PomA/PomB-F22Y+S27T (d) or PomA/PomB-F22Y+L35V (e) were measured as described in the legend of Fig. 2 in buffer containing 0–50 mM NaCl.

stator complex followed by the binding and release of the coupling ion will probably not occur. In other words, if the Na^+ binding pocket of PomA/B becomes properly coordinated to H^+ by mutagenesis, we should be able to produce an H^+-driven PomA/B complex. It has been shown clearly that the ion specificity can be changed by replacing some residues of MotB around the putative periplasmic entrance of the ion (Terahara *et al.*, 2008). Therefore, we changed the corresponding residues of PomB, but this had no effect on ion selectivity. Other amino acid residues of the periplasmic surface may be important for determining ion binding and specificity. Unfortunately, we could not identify the periplasmic surface residues which are involved in ion binding and specificity. However, we found that PomA-N194 may be important for ion specificity and may create an ion binding

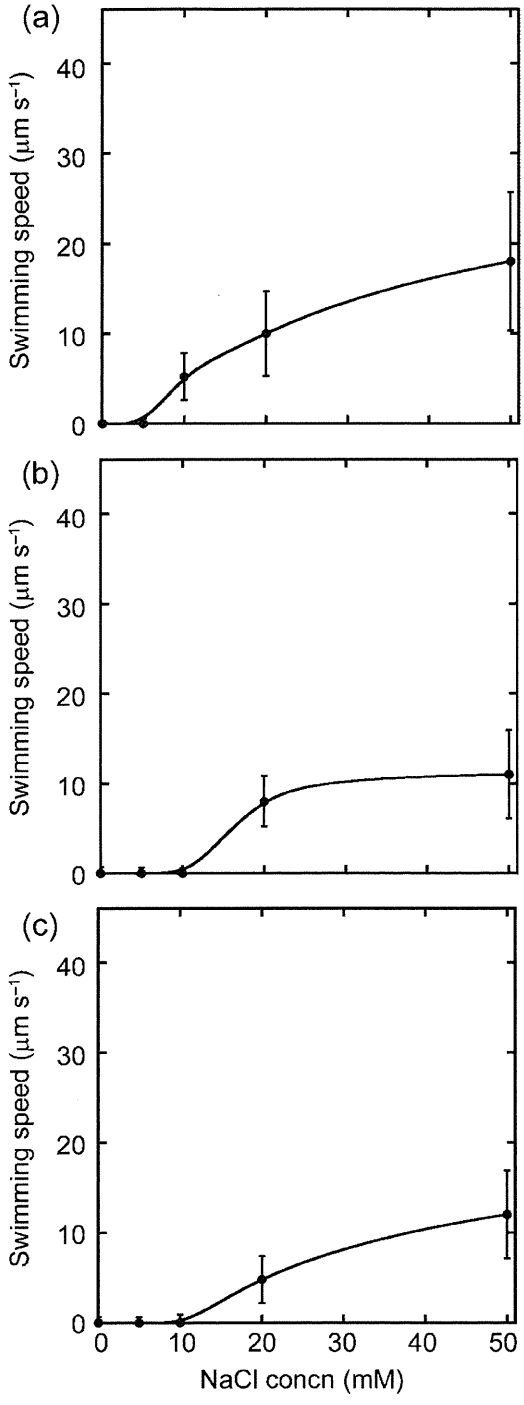

Fig. 5. Swimming speeds of various PomB-F22 mutants. Swimming speeds of cells producing F22A (a), F22S (b) or F22N (c) were measured as described in the legend of Fig. 2 in buffer containing 0–50 mM NaCl.

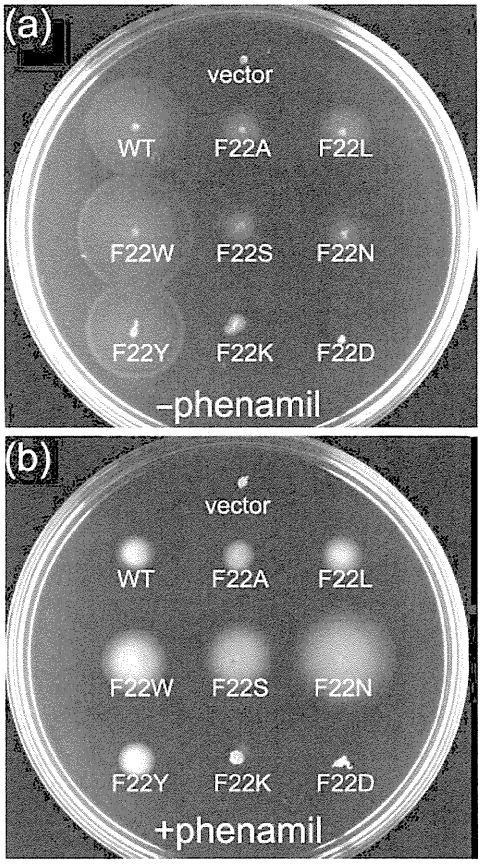

Fig. 6. Effects of phenamil on the swimming abilities of the various PomB-F22 mutants in semisolid agar. (a) Cells were inoculated on 0.25 % agar VPG plates and were incubated at 30 °C for 5 h. (b) Cells were inoculated on 0.25 % agar VPG plates containing 200 μM phenamil and were incubated at 30 °C for 24 h.

site with PomB-D24 at the central TM region. Some periplasmic surface residues may also contribute to the ion specificity. This means that the recognition mechanism for an ion is not simple and that multiple sites are necessary to determine the specificity, as discussed below.

In this study, we found that PomA-N194Y confers the ability to swim in an Na^+-free buffer in the increased motility strain sp2. However, we could not determine what the coupling ion is or whether the Na^+-type PomA/B has been converted to the H^+ type. Attenuated total reflection Fourier transform infrared spectroscopy has shown that the PomA/B complex has at least three Na^+ binding carboxyl residues. One of the Na^+ binding carboxyl residues is the essential aspartate, PomB-D24, and the others are as yet unidentified (Sudo *et al.*, 2009a). We suggest that other as-yet-unidentified Na^+ binding sites may contribute to determining the ion specificity and/or to promoting ion flow by efficient binding of the ions. Because PomA-N194 is thought to be the residue that forms the ion binding pocket with PomB-D24, the dramatic decrease of the swimming speed of cells expressing PomA-N194Y may derive from a slow flux of Na^+ because of inefficient recognition or binding of ions. The corresponding residue

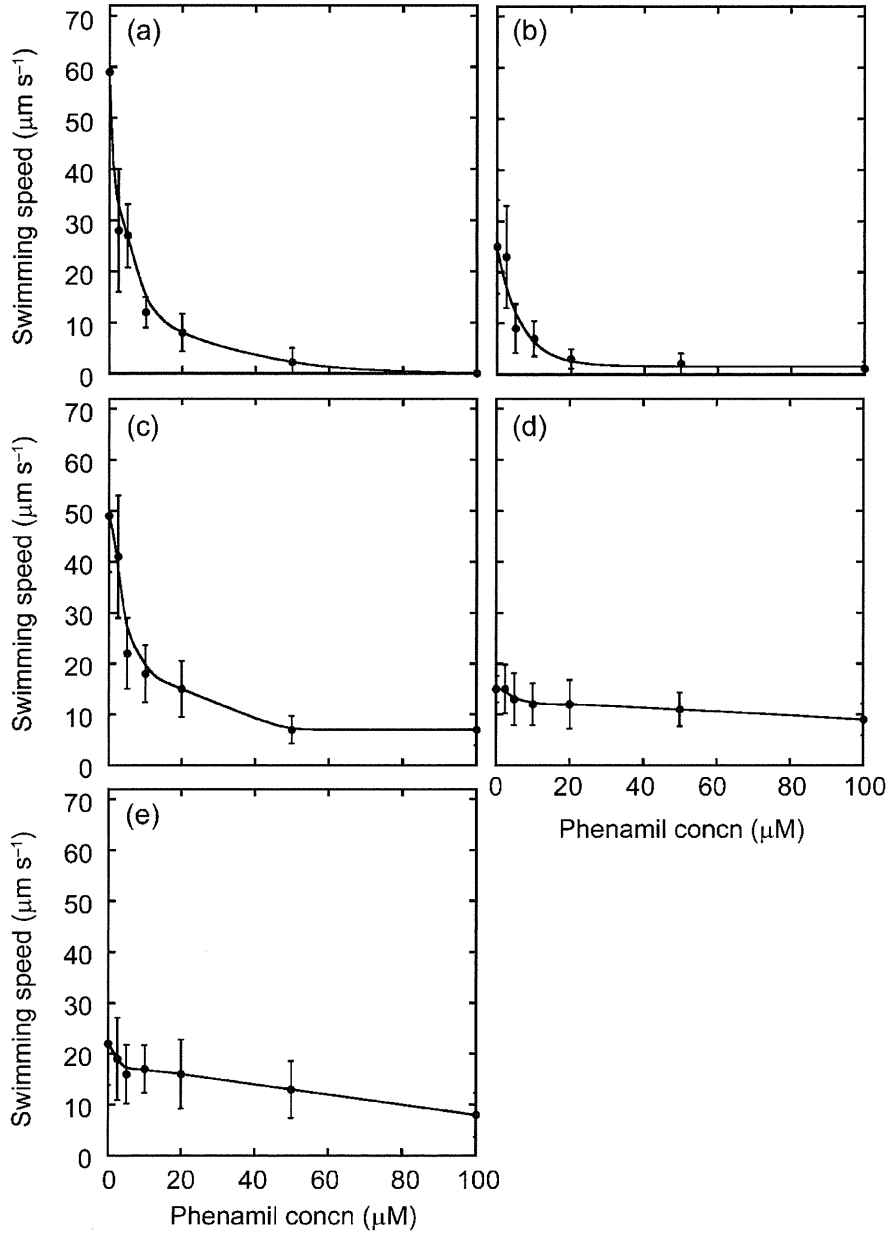

Fig. 7. Effects of phenamil on the swimming abilities of the various PomB-F22 mutants. Swimming speeds of cells producing PomB (a), PomB-F22Y (b), F22W (c), F22S (d) or F22N (e) were measured as described in the legend of Fig. 2 in buffer containing 300 mM NaCl and various concentrations of phenamil.

of the H^+-type MotA is conserved as tyrosine. This may imply that the tyrosine and/or asparagine contributes to the ion specificity (H^+ or Na^+) of the flagellar motor. We think that PomA-N194 might be one of the most important residues for ion specificity, although there are probably other residues that contribute. NtpK, which is a V-ATPase rotor ring component, coordinates Na^+ with the essential carboxyl group of E139, the carbonyl group of Q65 and Q110, the hydroxyl group of T64 and the main chain carbonyl group of L61 (Murata *et al.*, 2005). Therefore, we speculate that the ion binding pocket of PomA/B is composed of residues other than PomB-D24 and PomA-N194 that coordinate Na^+ ions. So, to generate an H^+-driven PomA/B complex, the introduction of two or more mutations with PomA-N194Y in TM4 may be required in other TM regions (TM1–3) of PomA.

It has been reported that the PomA-D31C mutant cells require a higher Na^+ concentration (greater than 19 mM NaCl) to exhibit swimming motility (Kojima *et al.*, 2000).

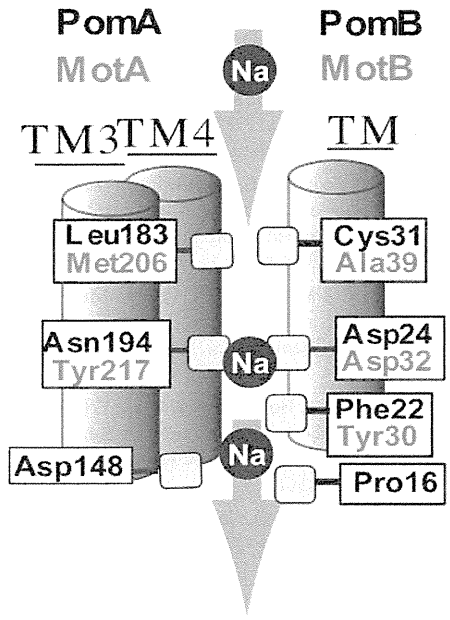

Fig. 8. Model of the ion flux pathway. Asp24 of PomB forms an Na^+ binding site which is suggested to make an ion binding pocket with Asn194 of PomA. Cys31 of PomB and Ala39 of MotB form a pair of amino acids for the H^+ and Na^+ channels with Leu183 of PomA and Met206 of MotA, respectively (Sudo *et al.*, 2009a, b; Terashima *et al.*, 2010). Phe22 of PomB is near an ion flow pathway and is close to the Na^+ binding site of Asp24, and might be involved in the release of Na^+ from PomB-D24. It has been suggested that PomA-D148 and PomB-P16 contribute to forming a high-affinity phenamil binding site at the inner face of the PomA/PomB complex.

When PomA-D31 was substituted to charge-inverted or large side-chain amino acids, the Na^+ thresholds of those mutants were even higher, above 50 mM NaCl. It has been speculated that the efficiency of Na^+ flow is increased by the negative charge at D31 and that Na^+ ions may be recruited by this negative charge. The motility of cells producing PomB-F22Y was decreased at low Na^+ concentration but did not change at high Na^+ concentration compared with the wild-type. We thus hypothesized that the F22Y mutation affects ion flux or torque generation. F22L, F22W and F22Y conferred almost the same maximal swimming speed as the wild-type, while the maximal swimming speeds of the F22A, F22S and F22N mutants were decreased to approximately 50 % of the wild-type value. The F22A, F22S and F22N mutants also showed a threshold of Na^+ concentration for swimming motility. On semisolid agar containing 500 mM NaCl, except for the F22L mutant, all swimming ring sizes correlated with the swimming speeds in the liquid. The size of the swimming ring of the F22L mutant was decreased to approximately 50 % of the wild-type value on semisolid agar, suggesting that torque might be reduced. The aromatic ring at position F22 might be important to generate maximal torque. In the F22Y mutant, the hydroxyl group of Tyr might lead to the motility defect under low Na^+ conditions. We speculate that the Na^+ flux might be reduced by the replacement of F22 in PomB with hydrophilic residues. In other words, the hydrophobicity at PomB-F22 is important to effectively release Na^+ from PomB-D24. On the other hand, in the H^+-driven motor, the residue corresponding to PomB-F22 is a conserved Tyr of MotB, implying that a hydroxyl group in this position is important for H^+ flux. We speculate that the aromatic ring at this position is important to generate a strong torque.

Aromatic amino acids are often found in ion channels and are important to regulate ion flow. It has been reported that the highly conserved Phe of voltage sensor proteins is important for channel function. For example, Phe233 of the Shaker K^+ channel might provide the rigid side chain on the structure and is important for its function. Among the residues replaced with various amino acids at Phe233, only two substitutions (Tyr and Trp) produce currents near wild-type levels with a negative V_m (midpoint voltage) (Tao *et al.*, 2010). We do not know whether the function of the Phe residue of Shaker is similar to that of Phe22 of PomB; however, aromatic amino acids may be used to maintain the size of the pore and to regulate ion flow in channels.

Cells expressing PomB-F22Y had a phenamil-resistant phenotype. It has been reported that the PomA-D148Y, PomB-P16S and PomB-A23S mutations, which are located on the cytoplasmic side of the TM segments, confer phenamil resistance upon the PomA/B complex, and it has been proposed that phenamil interacts with the cytoplasmic side of the ion-conducting pathway (Jaques *et al.*, 1999; Kojima *et al.*, 1999). Replacement of Phe22 in PomB with large hydrophobic (W) or hydrophilic residues (S and N) also conferred phenamil resistance upon the motor. Among these mutants, F22S and F22N had strong phenamil resistance. These results are consistent with the idea that Phe22 is involved in an ion-conducting pathway and is close to the Na^+ binding site.

PomB-F22Y would be on nearly the opposite helix face from PomB-D24 according to helical wheel modelling. However, a cross-linking study of MotA/B proposed that one MotA and one MotB subunit form an ion binding pocket and that the carboxyl group of MotB-D32 (corresponding to PomB-D24) directs ions to the pocket, although MotB-Y30 (corresponding to PomB-F22) is thought to face the other MotA subunit (Braun *et al.*, 2004). In the cross-linking study of TolQR, which are inner-membrane proteins of the Tol–Pal system that show homology with MotA/B and PomA/B, it has been proposed that TolR rotates between two TolQ subunits (Zhang *et al.*, 2009). If the TM region of PomB is also assumed to rotate among the TM regions between the two PomA subunits, even residues on the helix face opposite the PomB TM can orient to the helix face of the PomA TM segments.